JGR Solid Earth

RESEARCH ARTICLE
10.1029/2023JB027741

Glacial-Interglacial Circulation and Climatic Changes in the South Indian Ocean (Kerguelen Plateau Region) Recorded by Detrital and Biogenic Magnetic Minerals

Yan Liu[1,2,3,4], Catherine Kissel[5], Alain Mazaud[5], Yongxin Pan[1,4], and Jinhua Li[1,2,4]

[1]Key Laboratory of Earth and Planetary Physics, Institute of Geology and Geophysics, Chinese Academy of Sciences, Beijing, China, [2]Laboratory for Marine Geology, Qingdao National Laboratory for Marine Science and Technology, Qingdao, China, [3]Southern Marine Science and Engineering Guangdong Laboratory, Zhuhai, China, [4]University of Chinese Academy Sciences, Beijing, China, [5]Laboratoire des Sciences du Climat et de l'Environnement/IPSL, CEA, CNRS, UVSQ, Université Paris-Saclay, Gif-sur-Yvette, France

Key Points:

- Magnetic minerals in core MD11-3353 record paleoenvironmental changes in the South Indian Ocean over the past 150 Kyr
- Abundant detrital magnetic minerals illustrate an enhanced intensity of the Antarctic Circumpolar Current during the glacial periods
- Increased magnetofossils indicate an increased nutrient supply associated with the Southern Ocean upwelling during the interglacial periods

Supporting Information:

Supporting Information may be found in the online version of this article.

Correspondence to:

J. H. Li,
lijinhua@mail.iggcas.ac.cn

Citation:

Liu, Y., Kissel, C., Mazaud, A., Pan, Y., & Li, J. (2023). Glacial-interglacial circulation and climatic changes in the South Indian Ocean (Kerguelen Plateau region) recorded by detrital and biogenic magnetic minerals. *Journal of Geophysical Research: Solid Earth*, *128*, e2023JB027741. https://doi.org/10.1029/2023JB027741

Received 28 AUG 2023
Accepted 8 NOV 2023

Author Contributions:

Conceptualization: Jinhua Li
Data curation: Jinhua Li
Funding acquisition: Jinhua Li
Investigation: Yan Liu, Jinhua Li
Methodology: Jinhua Li
Project Administration: Jinhua Li
Resources: Catherine Kissel, Alain Mazaud, Jinhua Li
Supervision: Catherine Kissel, Jinhua Li
Visualization: Yan Liu, Jinhua Li
Writing – original draft: Yan Liu, Jinhua Li
Writing – review & editing: Catherine Kissel, Yongxin Pan, Jinhua Li

Abstract The Southern Ocean (SO) plays a fundamental role in global climate due to the presence of the intense eastward-flowing Antarctic Circumpolar Current (ACC), one of the most important ocean current systems. The configuration of the frontal systems of the ACC is controlled by the orbital- and millennial-scale variations of the Southern Hemisphere westerly winds (SHWW) and the SO upwelling. However, the reconstruction of paleoclimate and paleocurrent in the SO remains controversial possibly because of the complex interpretation of paleo-proxies and the regional variations. Here, we present results from rock magnetic measurements and electron microscopic analyses on marine core MD11-3353 over the past 150 Kyr, which is located in the Polar Front Zone, west of the Kerguelen Plateau. Our data sets indicate that magnetic mineral assemblages in the core are dominated by detrital magnetic minerals mixed with biogenic magnetic minerals (i.e., magnetofossils formed by magnetotactic bacteria) during the interglacial periods. Changes in the detrital magnetic mineral content indicate a strong modulation of the ACC intensity and the SHWW stress at the orbital scale over the last climatic cycle with an enhanced activity during the glacial periods. The increase in magnetofossils content during the interglacial periods indicates an enhanced nutrient supply from the SO upwelling resulting from the southward migration of the Antarctic Polar Front. Our results suggest that the variations of concentration and assemblage of magnetic minerals can be used as faithful proxies for reconstructing ocean circulation and upwelling changes in the South Indian Ocean over the past 150 Kyr.

Plain Language Summary The Southern Ocean plays a critical role in climate, ocean circulation, oceanic carbon sequestration, and nutrient distribution, in particular via the Antarctic Circumpolar Current (ACC), the largest wind-driven current on Earth. Reconstructing the past variability of the intensity and position of the ACC is challenging. Indeed, rather different results were obtained from different areas suggesting a strong regional dependence. In order to better decipher the mechanisms involved in the southern Indian sector, we performed detailed environmental magnetic analyses on a marine core collected west of the Kerguelen Plateau, presently under the influence of the ACC. Both detrital and biogenic magnetic minerals were identified over the past 150 Kyr, corresponding to the last climatic cycle. The temporal variations of detrital magnetic minerals suggest an enhanced intensity of the ACC during the glacial periods. In contrast, increased abundance of biogenic magnetic minerals during the interglacial periods indicates an increased nutrient supply associated with an enhanced Southern Ocean upwelling.

1. Introduction

The Southern Ocean (SO) plays a critical role in the global ocean circulation system with a deep influence on global climate through the Antarctic Circumpolar Current (ACC) (Studer et al., 2018). The ACC is the largest wind-driven current on Earth and connects the Atlantic, Pacific, and Indian Oceans in mid-southern latitudes (Marshall & Speer, 2012). The ACC southward shoaling brings deep waters to the ocean surface, controlling the nutrient delivery patterns and the oceanic carbon sequestration in the Southern Hemisphere (Ai et al., 2020; Anderson et al., 2009; Chang et al., 2023; Sigman & Boyle, 2000).

Along a north to south transect in the SO, the main ACC fronts include the Subantarctic Front (SAF), the Antarctic Polar Front (APF), and the Southern-ACC Front (Park et al., 2019; Rintoul & Naveira, 2013). The Polar

Front Zone (PFZ) is encompassed by the SAF and APF. It separates colder, nutrient-richer (Si, NO_3^-) Antarctic surface waters originating from the SO upwelling, from warmer, nutrient-poorer Subantarctic surface waters (Palter et al., 2013; Ragueneau et al., 2000). Past latitudinal variations of APF and therefore of ACC therefore influence the SO biogeochemistry and ecosystems (Kohfeld et al., 2005). It has been proposed that the latitudinal variations of the ACC were driven by changes in the Southern Hemisphere westerly winds (SHWW) during the last glacial-interglacial cycle (Toggweiler et al., 2006). However, the relationship between the ACC intensity and position and the glacial-interglacial climate remains elusive (McCave et al., 2014; Toyos et al., 2020). For instance, by analyzing the abundance and grain size of magnetic minerals in sediments from Southern Indian Ocean, Mazaud and coworkers proposed an enhanced ACC flow intensity during the glacial periods over the past ~500 Kyr (Mazaud et al., 2007, 2010). On the contrary, recent studies of sediments from the Drake Passage, based on the analysis of sedimentary grain sizes and geochemical signature, have suggested a reduced ACC flow intensity during the last glacial periods (Toyos et al., 2020; Wu et al., 2021). Numerous oceanographic surveys and numerical simulations have also been conducted (Graham et al., 2012; Kohfeld et al., 2013; Munday et al., 2013; Rojas et al., 2009; Saenko et al., 2005; Toggweiler et al., 2006). However, a consensus on temporal and spatial variations in SHWW stress, ACC flow intensity, and SO upwelling is still not reached most likely due to an underestimation of local processes impacting both numerical models and interpretation of proxies (Kohfeld et al., 2013). Therefore, new paleoclimate records are needed to provide a better understanding of the ACC intensity variability during the glacial-interglacial periods.

Magnetofossils are well-known biogenic magnetic minerals preserved in sediments or sedimentary rocks (Kirschvink & Chang, 1984; Kopp & Kirschvink, 2008; Pan et al., 2005; Roberts et al., 2012). They are actually fossil remains of magnetotactic bacteria (MTB), and promising recorders of paleoenvironmental information because of their ideal single domain (SD) nature and distinctive morphologies associated with different taxonomic MTB groups with contrasting habitat preferences (Li et al., 2013, 2021; Li, Liu, Wang, et al., 2020; P. Y. Liu et al., 2022; Pósfai et al., 2013). For instance, magnetofossil abundance and hematite flux changes have been used to indicate iron fertilization occurrence in open ocean settings (Roberts et al., 2011; Yamazaki & Ikehara, 2012). The grain size and crystal morphology of magnetofossils have been also interpreted to indicate organic supply increase and deep-water suboxic conditions in marine environments (Chang et al., 2018, 2023; Kopp & Kirschvink, 2008; Yamazaki & Kawahata, 1998). In the glacial-interglacial records, the fraction of such biogenic magnetic minerals was used, in combination with detrital magnetic mineral records, to constrain latitudinal variations of the Intertropical Convergence Zone in the eastern Pacific (Yamazaki, 2012).

In this study, we combine rock magnetic measurements and scanning/transmission electron microscopic observations on a sedimentary sequence (core MD11-3353) retrieved west of the Kerguelen Plateau (KP). We observe that variable concentrations of detrital and biogenic (i.e., magnetofossils) magnetic minerals faithfully illustrate the glacial-interglacial ACC intensity variability and/or the SO upwelling. This new magnetic mineral data set therefore provides new paleoceanographic and paleoclimatic information in the SO for the past 150 Kyr.

2. Materials and Methods

2.1. Marine Core Locations, Oceanographic Context, and Sampling

Core MD11-3353 (50°34.02′S, 68°23.13′E, 1,568 m water depth) was retrieved in 2011 with the long piston corer system (CALYPSO) on board the R/V *Marion Dufresne* during the MD185 INDIENSUD oceanographic expedition (Mazaud & Michel, 2011). The core site is located in the PFZ on the northwestern slope of the KP (Figure 1a), which is a large igneous province formed by mantle plume activity about 115 Ma ago (Whitechurch et al., 1992). The western margin of the KP is limited by the Crozet Plateau (CP) and Conrad Rise (CR), which were formed ~54 and ~75 Ma ago, respectively (Breton et al., 2013; Homrighausen et al., 2021). Mineralogical and geochemical analyses have suggested that these areas provide large amounts of volcanic detrital materials to the South Indian Ocean (SIO) (Bareille et al., 1994; Dezileau et al., 2000). The location of this core is close to the present APF.

Core MD11-3353, which mainly consists of siliceous ooze and siliciclastic mud was subsampled using u-channels (Weeks et al., 1993) for continuous high-resolution magnetic measurements at Laboratory of Sciences of Climate and Environment (Gif-sur-Yvette, France). On the basis of this continuous scan, representative samples were selected for rock magnetic measurements and electron microscopic analyses at the Institute of Geology and Geophysics, Chinese Academy of Sciences (IGG-CAS, Beijing, China).

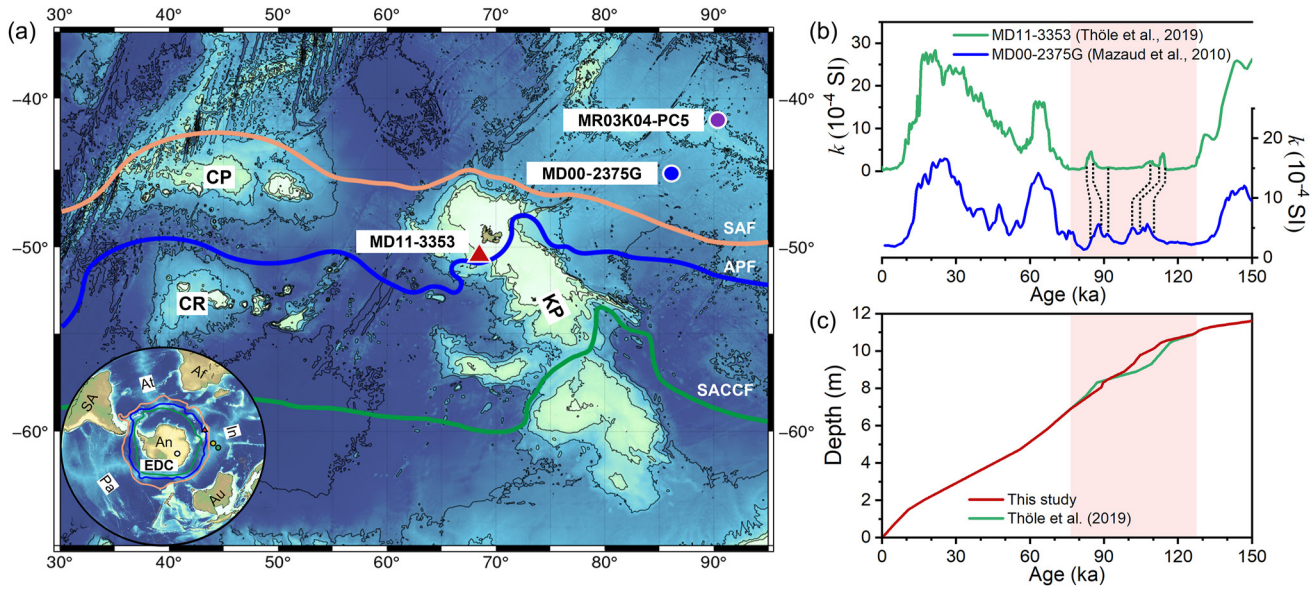

Figure 1. (a) Map of the studied South Indian Ocean area. The left-bottom inset in (a) shows the main components and positions of the Antarctic Circumpolar Current (ACC) in the Southern Ocean. The orange, blue, and green lines represent the Subantarctic Front (SAF), the Antarctic Polar Front (APF), and the Southern-ACC Front (SACCF), respectively. The main ACC fronts are drawn after Park et al. (2019). CP, Crozet Plateau; CR, Conrad Rise; KP, Kerguelen Plateau; EDC, EPICA Dome C ice core; SA, South America; Af, Africa; Au, Australia; An, Antarctica; At, Atlantic Ocean; In, Indian Ocean; Pa, Pacific Ocean. The red solid triangle indicates our study location (MD11-3353 core), while the blue and purple solid circles indicate the core locations of MD00-2375G (Mazaud et al., 2010) and MR03K04-PC5 (Yamazaki & Ikehara, 2012), respectively. (b) Magnetic susceptibility of core MD11-3353 and MD00-2375G reported versus its own age model from Thöle et al. (2019) (green line) and Mazaud et al. (2010) (blue line), respectively. The black dotted lines indicate the tie points used to adjust the age model from Thöle et al. (2019) to that of Mazaud et al. (2010) within Marine Isotope Stage 5 (period highlighted by the light orange rectangle). (c) The age-depth model of Thöle et al. (2019) (red line) and this study (green line) for core MD11-3353 over the last 150 Kyr.

The two other cores to which we compare our results (Figure 1a) are core MD00-2375G, composed of carbonate oozes (Dezileau et al., 2000; Mazaud et al., 2010), and core MR03K04-PC5 dominated by foraminifera-bearing nannofossil ooze (Yamazaki & Ikehara, 2012).

2.2. Room-Temperature Magnetic Measurements

Volume low-field magnetic susceptibility (κ) and anhysteretic remanent magnetization (ARM) measurements were performed at 2 cm intervals on u-channels with the spatial resolution of ~5.6 cm. A Bartington MS2C 45 mm internal diameter coil device was used for κ measurements. A 2G cryogenic magnetometer equipped with high-resolution pick-up coils was used for ARM measurements induced using a 100 mT alternating field, and a 0.05 mT direct current (DC) bias field.

A total of 23 samples were selected for rock magnetic measurements on a vibrating sample magnetometer (Princeton MicroMag model 3900, sensitivity = 5×10^{-10} Am^2). First, hysteresis loops were measured on maximum applied fields of 1 T with a 5 mT increment. Saturation magnetization (M_s), saturation remanent magnetization (M_{rs}), and coercivity (B_c) were obtained after applying high-field (>700 mT) slope corrections to remove the contributions of diamagnetic/paramagnetic minerals. Second, static isothermal remanent magnetization (IRM) acquisition curves were measured with 120 measurement points based on nonlinear field steps on a log scale (up to 1 T). Then, IRM acquisition curves were decomposed into cumulative log-Gaussian curves (Robertson & France, 1994) following the protocol of Kruiver et al. (2001). The remanence coercivity (B_{cr}) was determined from the DC demagnetization (DCD) curve of saturation IRM ($SIRM_{1T}$) back to −1 T. The hard IRM (HIRM) and S-ratio were defined as ½($SIRM_{1T}$ + IRM_{-300mT}) and −IRM_{-300mT}/$SIRM_{1T}$, respectively. The *R*-value of the Wohlfarth-Cisowski test, used to characterize magnetic interactions (Cisowski, 1981), was determined as the cross point between normalized IRM acquisition (i.e., IRM(H)/SIRM) and rescaled SIRM DCD curves (i.e., ½(1 + IRM(−H)/SIRM)). Finally, first order reversal curves (FORCs) (Egli et al., 2010; Pike et al., 1999; Roberts et al., 2000) were measured with a positive saturation field of 1 T, an increasing field step (δH) of 0.856 mT, and a 300 ms average time. FORC data processing were carried out using the FORCinel v3.06 software package

and smoothed by the VARIFORC algorithm (Sc0 = 7, Sc1 = 7, Sb0 = 6, and Sb1 = 7) (Egli, 2013; Harrison & Feinberg, 2008).

2.3. Low-Temperature Magnetic Measurements

Zero-field-cooled (ZFC) and field-cooled (FC) curves were performed on a Quantum Design Magnetic Property Measurement System (MPMS XP-5, sensitivity = 5×10^{-10} Am^2). Cooling samples from 300 to 10 K in zero field and in a 2.5 T field were used for ZFC and FC analyses, respectively. Then $SIRM_{10\ K\_2.5\ T}$ from 10 to 300 K in zero field was measured. The Verwey transition temperature (T_v) is defined as a negative peak in the first-order derivative of the FC curve, while the δ-ratio is defined as δ_{FC}/δ_{ZFC}, where δ is calculated as $(M_{80K} - M_{150K})/M_{80}$ and M_{80K} and M_{150K} represent remanences at 80 and 150 K, respectively (Moskowitz et al., 1993).

2.4. Electron Microscopic Analyses

Sixteen of the 23 sediment samples were further picked out for magnetic extraction and subsequent electron microscopic characterization following the protocol described by Li, Liu, Liu, et al. (2020). The extracted magnetic minerals were deposited on carbon-coated copper transmission electron microscope (TEM) grids for both large-area scanning electron microscope (SEM) and high-resolution TEM (HRTEM) observations (Li, Liu, Liu, et al., 2020). SEM experiments were carried out with Thermoscientific Apreo microscope equipped with a field emission gun electron source and a Bruker XFlash 60 energy dispersive X-ray spectrometer (EDXS). Lattice imaging by HRTEM, mineral identification by selected-area electron diffraction (SAED), and chemical micro-analysis by EDXS were performed at an accelerating voltage of 200 kV on a JEOL JEM-2100HR microscope equipped with a LaB_6 gun electron source and an X-Max EDXS detector.

2.5. Age Model

The age model of core MD11-3353 was constructed by Thöle et al. (2019) via the correlation of MD11-3353 $TEX^{86}L$ sea surface temperatures data with a well-dated stable hydrogen isotope (δD) record of EPICA Dome C (EDC) ice core (Figure 1a) (Jouzel et al., 2007). The entire core covers about 400 Kyr with a relatively constant average sedimentation rate of ~7.5 cm Kyr^{-1}. In this paper, we focus on the past ~150 Kyr from Marine Isotopic stage (MIS) 6 to the present.

The other two cores (i.e., MD00-2375G and MR03K04-PC5) (Figure 1a) were dated via comparison of their planktonic stable oxygen isotope ($\delta^{18}O$) record with the δD record of EDC ice core for core MD00-2375G (Mazaud et al., 2010), and with the SPECMAP stack for core MR03K04-PC5 (Yamazaki & Ikehara, 2012). Within MIS 5, because the $TEX^{86}L$ could not accurately resolve the various substages (Pugh et al., 2009), we used the susceptibility variations to transfer the age model of core MD00-2375G to MD11-3353 with six different tie points using AnalySeries software (Paillard et al., 1996) (Figure 1b). We thus refined the Thöle et al. (2019) age model within MIS 5, leading to a smoother depth/age relationship (Figure 1c).

The 23 selected samples were classified by MIS and numbered from young to old. For example, S5-3 indicates the third sample during MIS 5 and S5-4 is older than S5-3. One sample was taken in the Holocene, a second one in Termination I (T1) and a third one in MIS 2. Three, three, twelve, and two samples were collected in the intervals corresponding to MIS 3, 4, 5, and 6, respectively (Figure 2c). The 12 samples collected from MIS 5 are distributed in all substages from MIS 5a to MIS 5e (Figure 2).

3. Results

3.1. Temporal Variation of Magnetic Mineral Concentration

The magnetic parameters κ, ARM, M_s, $SIRM_{1T}$, and HIRM, which are related to the concentration of magnetic minerals, have similar temporal variation patterns throughout the core (Figures 2a–2e). They show a gradual decrease during the late MIS 6 and remain at their lowest values for most part of MIS 5, but with two slight increases in the MIS 5d and MIS 5b cold substages. They then increase gradually from the late MIS 5a to MIS 2, with a big hump in the middle part of MIS 4, and reach their highest values at ~18–25 Kyr, which roughly coincides with the Last Glacial Maximum. They decrease rapidly during Termination I (T1) from ~18 to ~10 Kyr,

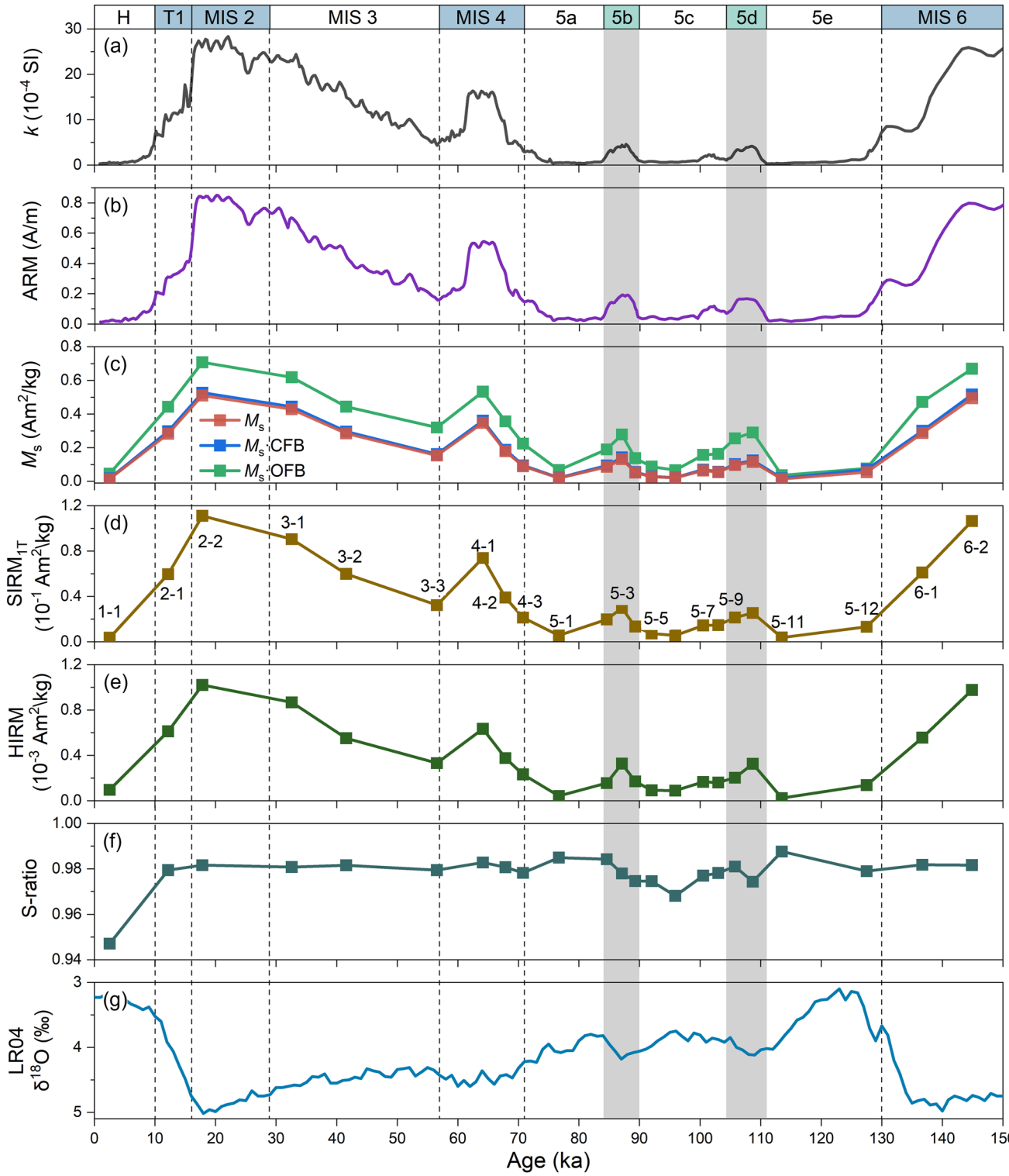

Figure 2. Temporal variations of concentration-dependent magnetic parameters for MD11-3353 core over the past 150 Kyr. (a) κ, low-field magnetic susceptibility. (b) ARM, anhysteretic remanent magnetization. (c) Saturation magnetization (M_s) (red line), M_s plotted on a carbonate-free basis (M_s·CFB) (blue line) and opal-free basis (M_s·OFB) (green line). (d) $SIRM_{1T}$, saturation isothermal remanent magnetization acquired in a 1T field. (e) HIRM, hard isothermal remanent magnetization. (f) S-ratio, $-IRM_{-300mT}/SIRM_{1T}$. (g) LR04 benthic $\delta^{18}O$ stack (Lisiecki & Raymo, 2005). Gray shadings outline the cold substages during Marine Isotope Stage (MIS) 5. Both κ and ARM were obtained from u-channels at 2 cm interval with a resolution of 5.6 cm, while M_s, $SIRM_{1T}$, HIRM, and S-ratio were obtained from the 23 selected samples from the core. The numbers in (d) correspond to the sample labeling.

to finally reach their lowest values again in the Holocene. In summary, the concentration in magnetic minerals is relatively low during the Holocene and the relatively warm substages MIS 5a, MIS 5c, and MIS 5e and relatively high during the glacial periods (i.e., MIS 6, MIS 4 to MIS 2, and T1) and the relatively cold MIS 5b and MIS 5d substages. In the detailed study by Thöle et al. (2019), many proxies have been analyzed. In particular, the authors report on opal and calcium carbonate content which may play the role of dilutant of the magnetic fraction. We have calculated for all the studied samples the M_s values on carbonate-free and opal-free basis using the formula: M_s·X-free basis = $M_s \times 100/(100 - X\%)$, where X is for carbonate or opal. As shown in Figure 2c, these two calculated curves still show similar temporal variations as our magnetic concentration record. This demonstrates that the temporal variation pattern of the magnetic content does not result from a dilution by the main non-magnetic fractions.

The S-ratio, which is the most sensitive parameter for estimating the relative amount of high-coercivity minerals (e.g., hematite and goethite) and low-coercivity minerals (e.g., magnetite, maghemite) (King & Channell, 1991; Q. S. Liu et al., 2012), keeps relative stable around 0.98 during most part of the glacial periods (e.g., MIS 6, MIS 4 to MIS 2, and T1) and small amplitude oscillations (down to 0.96) during the MIS 5 and early MIS 4 (Figure 2f). These values very close to 1 indicate that the remanence of the core sediments is mainly carried by low-coercivity magnetic minerals, consistently with the relative low HIRM values compared to $SIRM_{1T}$ (Figure 2e).

3.2. Temporal Variation of Magnetic Mineral Assemblage

We tested the presence of magnetite in core MD11-3353 using low-temperature magnetic measurements. As shown in Figure 3, both FC and ZFC warming curves show a weak but detectable Verwey transition between ~90 and ~120 K for all detected samples, indicating the presence of magnetite (Muxworthy & McClelland, 2000). Most samples from the glacial periods and from the warm substages of MIS 5 tend to have only one major transition peak at ~110 and ~97 K, respectively (Figures 3a and 3g). Comparatively, samples from the cold substages of MIS 5 (i.e., S5-9) and early MIS 4 (i.e., S4-2) tend to have a plateau-like form between ~97 and ~110 K (Figures 3d and 3j). Generally, a reduced T_v value for detrital inorganic magnetite means an impure chemical composition (i.e., nonstoichiometry) (Muxworthy & McClelland, 2000), or an oxidative modification (i.e., maghemitization) (Yamazaki, 2008), or both. Biogenic magnetite produced by MTB is usually characterized by T_v values lower than ~110 K (Li, Menguy, Leroy, et al., 2020; Moskowitz et al., 1993). Therefore, a plateau-like form between ~97 and ~110 K around T_v observed in marine sediment samples has been used as evidence for a mixture of detrital inorganic magnetites and magnetofossils (Chang, Heslop, et al., 2016).

The magnetic mineral assemblages in the 23 selected sediment samples were further characterized by hysteresis loop, IRM acquisition/demagnetization, and FORC experiments (Figure 3 and Figures S1–S12 in Supporting Information S1). All the measured samples have narrow hysteresis loops and IRM acquisition curves largely increasing at low field to reach a nearly saturated state at ~300 mT. This is consistent with the S-ratio and confirms the dominance of low-coercivity magnetic minerals. Normalized IRM acquisition and SIRM DCD curves are roughly symmetric and cross each other at a calculated R-value ranging from 0.44 to 0.47 (Figures 3b, 3e, 3h, and 3k; Table S1 in Supporting Information S1). This suggests that the magnetic minerals weakly interact (Cisowski, 1981). The SD and vortex states of the magnetic minerals are well characterized by their corresponding FORC diagrams (Egli et al., 2010; Roberts et al., 2017). Comparatively, most samples from the glacial periods and the cold substages of MIS 5 tend to have a butterfly-like FORC distribution for the vortex structure (Figures 3c, 3f, 3l), while the samples from the warm MIS5 substages tend to have a ridge-shaped FORC distribution for weakly interacting SD particles (Figure 3i).

The rock magnetic measurements we conducted on the 23 selected samples also allow to analyze the temporal variation of the magnetic grain size (e.g., κ_{ARM}/κ, B_c, B_{cr}, M_{rs}/M_s, and B_{cr}/B_c) and of the abundance of magnetofossils (e.g., δ_{FC}, δ_{ZFC}, and δ_{FC}/δ_{ZFC}) (Li, Menguy, Leroy, et al., 2020; Moskowitz et al., 1993). As shown in Figure 4, the κ_{ARM}/κ, B_c, B_{cr}, M_{rs}/M_s, and δ_{FC}/δ_{ZFC} values are lower, and the B_{cr}/B_c, δ_{FC}, and δ_{ZFC} values are higher for most of sediment samples during the glacial periods (e.g., MIS 6, MIS 4 to MIS 2, and T1) compared to MIS 5 and Holocene. This indicates that the magnetite assemblages are made of relatively coarser magnetic grains and relatively lower magnetofossils content during the glacial periods than during interglacial ones (Day et al., 1977; Dunlop, 2002; Li, Menguy, Leroy, et al., 2020; Q. S. Liu et al., 2012; Moskowitz et al., 1993; Peters & Dekkers, 2003). Within MIS 5, all these magnetic parameters oscillate with higher (lower) values of κ_{ARM}/κ, B_c, B_{cr}, and M_{rs}/M_s, δ_{FC}/δ_{ZFC}, and lower (higher) values of B_{cr}/B_c, δ_{FC}, and δ_{ZFC} during the relatively warm (cold)

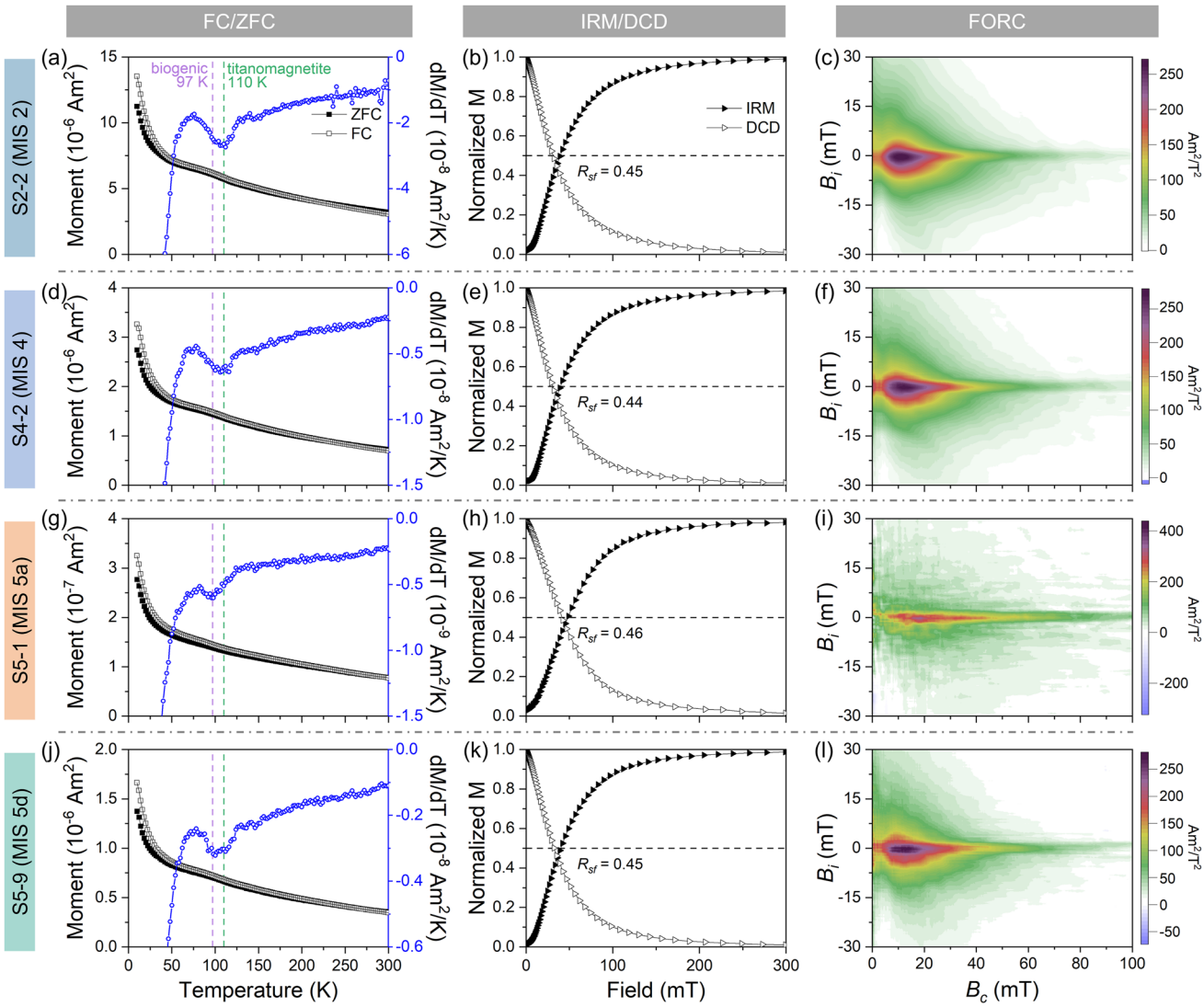

Figure 3. Rock magnetic measurements of four representative samples selected from the glacial periods MIS 2 (S2-2, (a–c)) and early MIS 4 (S4-2, (d–f)), the warm substage MIS 5a (S5-1, (g–i)), and the cold substage MIS 5d (S5-9, (j–l)) during the interglacial period MIS 5. The first, second, and third columns are FC-$SIRM_{10K\_2.5T}$ and ZFC-$SIRM_{10\ K\_2.5T}$ warming curves, normalized IRM acquisition and $SIRM_{1T}$ direct current demagnetization (DCD) curves, and first order reversal curve (FORC) diagrams, respectively. The blue lines with white circles in panels (a, d, g, and j) are the first-order derivative curves of field-cooled (FC). Purple and green dashed lines indicate the temperature points of ~97 and ~110 K, respectively. Results of rock magnetic measurements on more samples are provided in Figures S1–S12 in Supporting Information S1.

substages. This indicates finer (coarser) magnetic grains and more magnetofossils remain during the relatively warmer substages.

In summary, both room- and low-temperature magnetic measurements consistently suggest that magnetite or/and maghemite particles are coarser during glacial periods than during interglacial periods. In addition, both FORC diagrams and hysteresis loops demonstrate that these magnetite or/and maghemite particles are dominated by the SD and vortex states across this core, and that superparamagnetic fractions should be very small, which is consistent with the previous studies in this region (Manoj et al., 2012; Mazaud et al., 2010).

3.3. Results of Electron Microscopic Observations

SEM and TEM approaches were combined to precisely identify assemblages and origins of the magnetic minerals in core MD11-3353 (Figure 5 and Figures S13–S31 in Supporting Information S1). Six types of magnetite

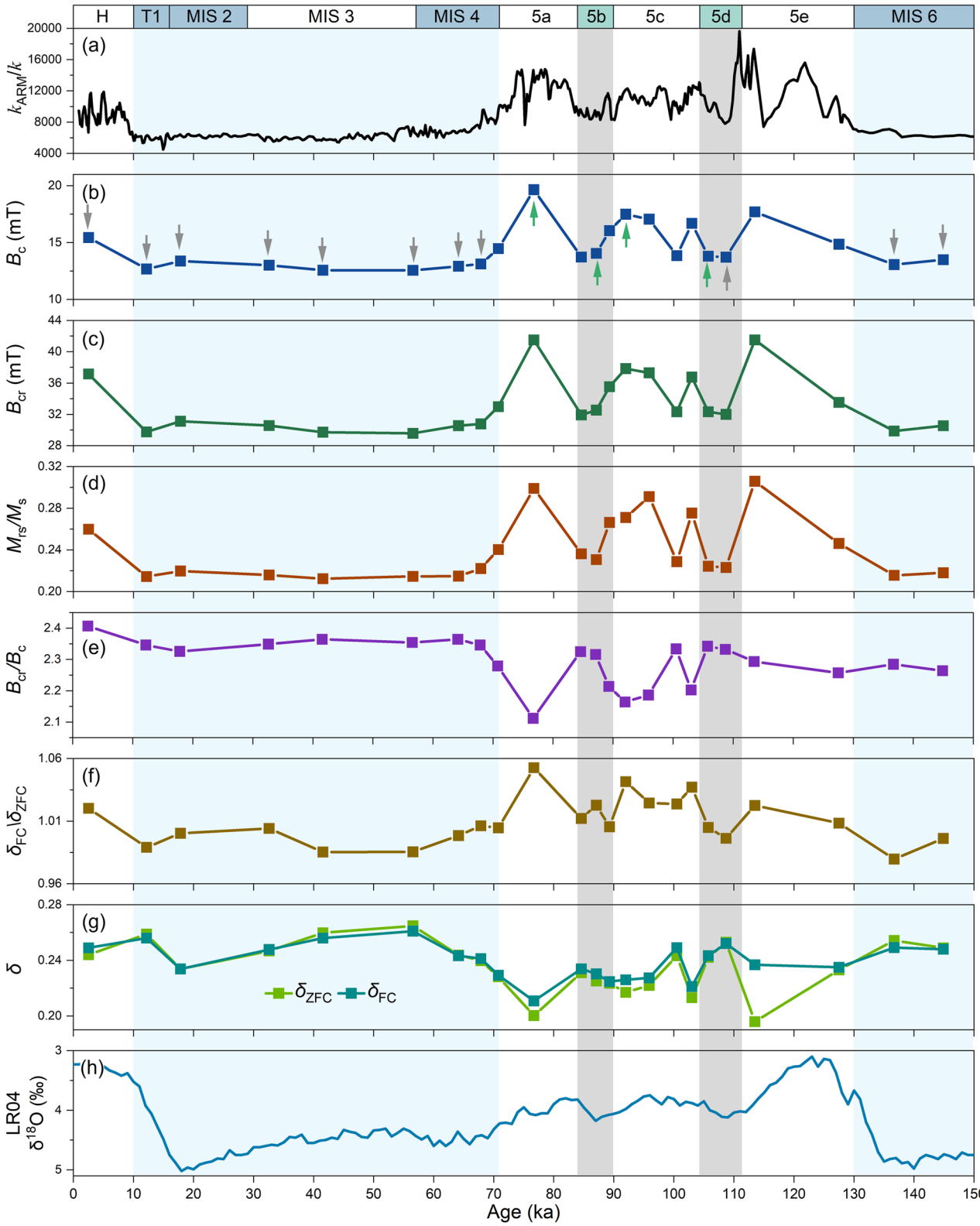

Figure 4.

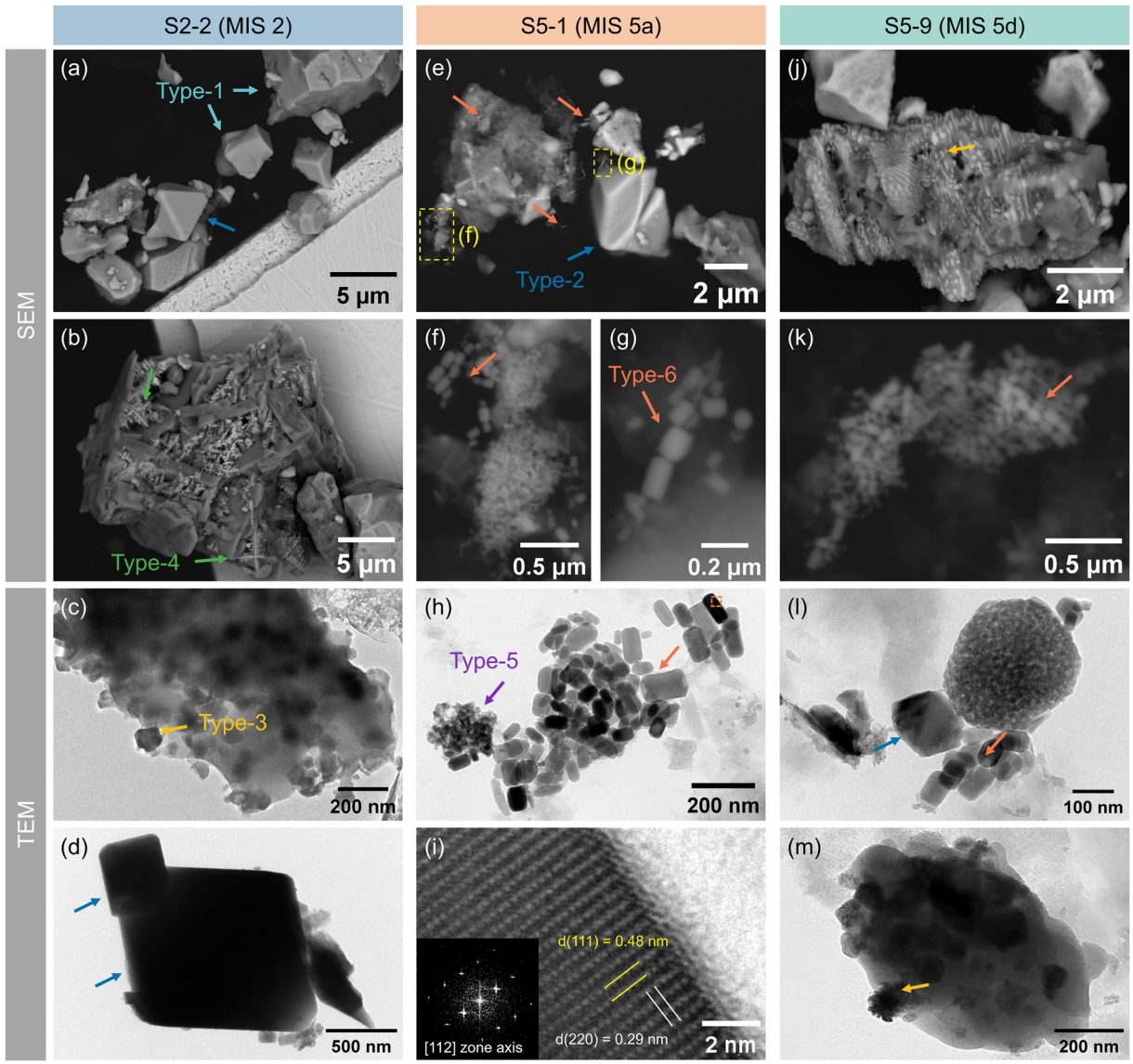

Figure 5. Electron microscopic characterization of magnetic minerals in three representative samples from MIS 2 (S2-2, (a–d)), MIS 5a (S5-1, (e–i)), and MIS 5d (S5-9, (j–m)). The top and bottom two rows are scanning electron microscope (SEM) and transmission electron microscope (TEM) images, respectively. Five types of detrital titanomagnetite minerals (Types 1–5) are indicated by solid arrows with different colors: cyan for Type-1, irregular or angular magnetites (a); blue for Type-2, octahedral magnetites (d and e); yellow for Type-3, silicate-hosted irregular or cubic magnetites (c, j, and m); green for Type-4, silicate-hosted dendritic-like magnetites (b); and purple for Type-5, tight aggregates of nanometer-sized superparamagnetic titanomagnetites (h). Magnetofossils (Type-6) are indicated by solid orange arrows (e–l). Panel (i) is high-resolution TEM image (inset is the corresponding Fast Fourier Transform pattern) of one magnetofossil particle indicated by the orange dashed box in (h). Systematic electron microscopic characterization of the other samples is provided in Figures S13–S31 in Supporting Information S1.

particles could be identified based on the combination of SEM, TEM and HRTEM imaging, and SAED and TEM-based EDXS analyses (Li, Liu, Liu, et al., 2020). Type-1 and Type-2 are well-defined octahedral particles with irregular and angular shapes, respectively. Both types often have grain sizes that range from a few hundred nanometers to a few microns. Type-3 corresponds to irregular or cubic particles and has grain sizes usually ranging from tens to hundreds of nanometers. Type-4 is micron-sized magnetite that are assembled in dendritic-like

Figure 4. Temporal variations of magnetic parameters from core MD11-3353 over the past 150 Kyr. (a) κ_{ARM}/κ, (b) B_c, coercivity, (c) B_{cr}, remanence coercivity, (d) M_{rs}/M_s, (e) B_{cr}/B_c, (f) δ_{FC}/δ_{ZFC}, and (g) δ_{ZFC} and δ_{FC}. (h) LR04 benthic $\delta^{18}O$ stack (Lisiecki & Raymo, 2005). The κ_{ARM}/κ was obtained from u-channels at 2 cm interval, while B_c, B_{cr}, M_{rs}/M_s, B_{cr}/B_c, δ_{FC}/δ_{ZFC}, δ_{ZFC}, and δ_{FC} were obtained from the 23 selected samples from the core. Solid gray and green arrows in (b) represent the 16 discrete samples picked out for electron microscopic analyses (Figure 5 and Figures S13–S31 in Supporting Information S1). Solid green arrows are the four typical samples selected for statistical analyses of magnetofossils morphology shown in Figure 6. Light blue and gray shadings outline the glacial periods (i.e., MIS 6, MIS 4-2, and T1) and the cold substages during MIS 5 (i.e., MIS 5d and 5b), respectively.

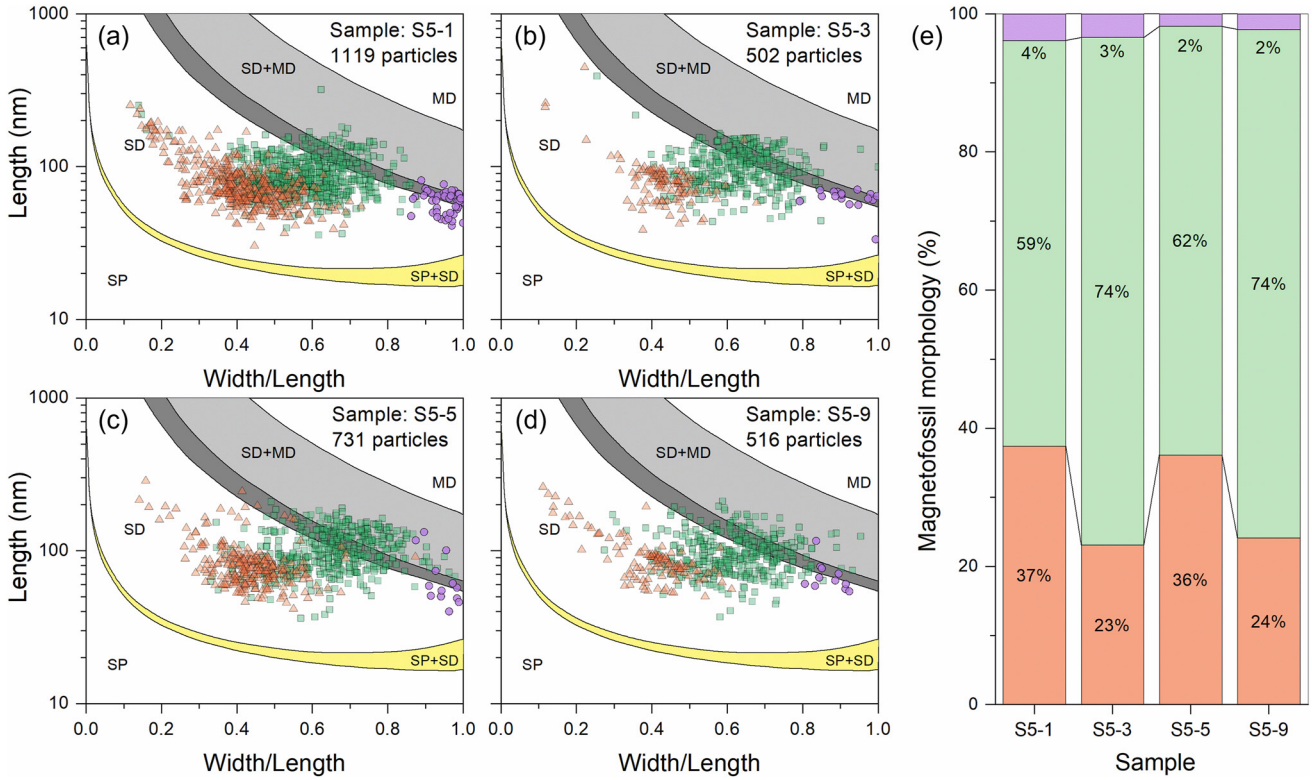

Figure 6. (a–d) Grain size distributions of magnetofossils with three types of morphologies observed in four sediment samples from the warm (a, c) and cold (b, d) substages of MIS 5 are plotted in the theoretical domain state phase diagram (Muxworthy & Williams, 2009). Cuboctahedral (purple solid circles), elongated prismatic (green solid squares), and bullet-shaped (orange solid triangles). (e) Proportions of cuboctahedral (purple shading), elongated prismatic (green shading), and bullet-shaped (orange shading) magnetofossils in the four samples.

structures. Both Type-3 and Type-4 particles are generally hosted within silicates. Type-5 is magnetite aggregates consisting of many nanometer-sized particles. Integrated use of various TEM techniques on individual particles reveals that these five types are titanomagnetites with variable Ti contents (Figures S13–S31 in Supporting Information S1). They most likely originate from detrital input from the SO land masses (e.g., CP, CR, and KP) (Bareille et al., 1994; Dezileau et al., 2000). Type-6 magnetites were readily recognized as magnetofossils (i.e., biogenic magnetites) because they have typically morphological, crystallographic, and chemical features that are identical to magnetosome magnetites produced by modern MTB (Figures S13–S31 in Supporting Information S1). Indeed, they have narrow grain size distributions (generally ranging from ~30 to ~200 nm) and well-defined crystal morphologies (including abundant elongated prisms and bullet shapes, and a small amount of cuboctahedrons). We also observe the presence of short chains with a few particles with the same morphology, and chemical structures with only Fe and O without any other detectable elements such as Ti (Li et al., 2013; Li, Menguy, Leroy, et al., 2020). In addition, HRTEM on individual particles showed that almost all of the detected magnetofossils still maintain well-defined crystal faces and nearly perfect lattice structures (Figure 5i). This suggests that the magnetofossils have been well preserved in this core and did not suffer from any strong diagenetic alteration (Roberts, 2015; Yamazaki et al., 2020).

The detected detrital titanomagnetites (Type-1 to Type-5) and magnetofossils (Type-6) vary in abundance between the glacial and interglacial periods (Figures S13–S31 in Supporting Information S1). In most samples from the glacial periods, Type-1 to Type 4 detrital titanomagnetite particles were readily observed by both SEM and TEM observations, while very few magnetofossils were occasionally found and only by TEM observations. In contrast, both detrital titanomagnetites and magnetofossils appear with roughly equal probability in most samples from the interglacial periods and early MIS 4. Partially collapsed magnetofossil chains were observed using both SEM and TEM (Figure 5 and Figures S13–S31 in Supporting Information S1). It should be noted that the Type-5 detrital titanomagnetite aggregates could be observed only by TEM in some glacial and interglacial samples (Figure 5h), possibly due to their low abundance and small sizes.

The morphological types of magnetofossils during MIS 5 were further statistically analyzed in four typical samples from the warm (e.g., S5-1 and S5-5) and cold (e.g., S5-3 and S5-9) substages (Figure 4). The crystal length (along the long axis) and width (perpendicular to the long axis) of nearly 3,000 magnetofossils were manually measured on ~300 TEM images with the Image J software package (https://imagej.nih.gov/ij/). TEM observations and statistical analyses showed that the magnetofossils are dominated by elongated prismatic and bullet-shaped magnetites with a small proportion of cuboctahedral magnetite (<4%). Comparatively, the proportion of bullet-shaped magnetofossils significantly increases to ~36% (S5-5) and ~37% (S5-1) during the warm substages, while it is ~23% (S5-3) and ~24% (S5-9) during the cold substages.

In a word, detailed electron microscopic observations of the magnetic extracts are well consistent with bulk rock magnetic measurements. Both demonstrated that core MD11-3353 is dominated by detrital titanomagnetites only mixed with magnetofossils during the interglacial periods and early MIS 4. This accounts well for relatively coarse magnetic grains during the glacial (and cold periods of MIS5) and a fining of the magnetic assemblage during the interglacial periods (in particular, the relatively warm MIS substages) by the addition of a substantial amount of magnetofossils.

4. Discussion

4.1. Occurrence and Temporal Variations of Detrital and Biogenic Magnetic Minerals

IRM decomposition has been widely used in environmental magnetism to quantify the different magnetic components of a mixture based on their different mean coercivity spectra (Egli, 2004; Heslop et al., 2002; Q. S. Liu et al., 2012). However, recent studies revealed that such method is by no means straightforward for quantitatively identifying a mixture of detrital and biogenic magnetites mainly because of the widespread distribution of silicate-hosted, nanometer-sized magnetite inclusions in marine sediments, which could produce similar coercivity to that of magnetofossils (Chang, Roberts, et al., 2016; Jiang et al., 2021; Li, Liu, Liu, et al., 2020). Both experimental and simulation studies have well documented that the coercivity of magnetosomes is also related to the grain size, crystal morphology, and spatial arrangement of the particles (Berndt et al., 2020; Chang et al., 2019; Li, Menguy, Leroy, et al., 2020). By the combination of rock magnetic measurements and electron microscopic observations, this study reveals that the sediment from core MD11-3353 are dominated by detrital titanomagnetites (including micron-, submicron- and nanometer-sized discrete and silicate-hosted titanomagnetites) during the glacial periods, and by a mixture of detrital and biogenic (mainly including elongated prismatic and bullet-shaped magnetite-type magnetofossils) magnetites during the interglacial periods. Given all these considerations, we have still tried to decompose the IRM acquisition curves with three, four, and five magnetic coercivity components to test the temporal variations of magnetic assemblages over the past 150 Kyr (Figure S32 in Supporting Information S1). IRM unmixing results show that all coercivity components, no matter which unmixing strategy is taken, are relatively stable during most part of the glacial periods, and oscillate during the interglacial period and early MIS 4 (Figures S33–S35 in Supporting Information S1). Among them, one component (i.e., Comp 2 with coercivity midpoint ($B_{1/2}$) ranging from ~47 to ~54 mT, Comp 3 with $B_{1/2}$ ranging from ~47 to ~58 mT, and Comp 4 with $B_{1/2}$ ranging from ~60 to ~71 mT in case of three-, four-, and five-components unmixing strategies, respectively) significantly increases during the interglacial periods with a variation pattern identical to that of κ_{ARM}/κ, B_c, B_{cr}, and M_{rs}/M_s. In turn, all other components clearly decrease (Figures S33–S35 in Supporting Information S1). IRM unmixing results confirm that the magnetic mineral assemblage is relatively stable during the glacial periods (with the exception of the early MIS 4), although the concentrations of magnetic minerals changed significantly. Moreover, the electron microscopic observations have suggested that the content of magnetofossils with abundant elongated prisms and bullet shapes, and a small amount of cuboctahedrons increased during interglacial periods, corresponding to the coercivity component with $B_{1/2}$ ranging from ~47 to ~71 mT (i.e., Comp 2, Comp 3, and Comp 4 in case of three-, four-, and five-components unmixing strategies, respectively) (Egli, 2004; Li, Menguy, Leroy, et al., 2020). Therefore, the addition and variation of magnetofossils during the interglacial periods and early MIS 4 may affect the temporal variations of these coercivity component. However, it should be noted that such coercivity components within sediment samples during both glacial and interglacial periods also contain contribution from time-varying detrital titanomagnetites (e.g., nanometer-sized and silicate-hosted magnetic inclusions).

Considering the M_{rs}/M_s of one sample from the warm period of MIS 5 interglacial periods and the early MIS 4 being a simple weighting from biogenic (magnetofossils) and detrital magnetic minerals, one could roughly

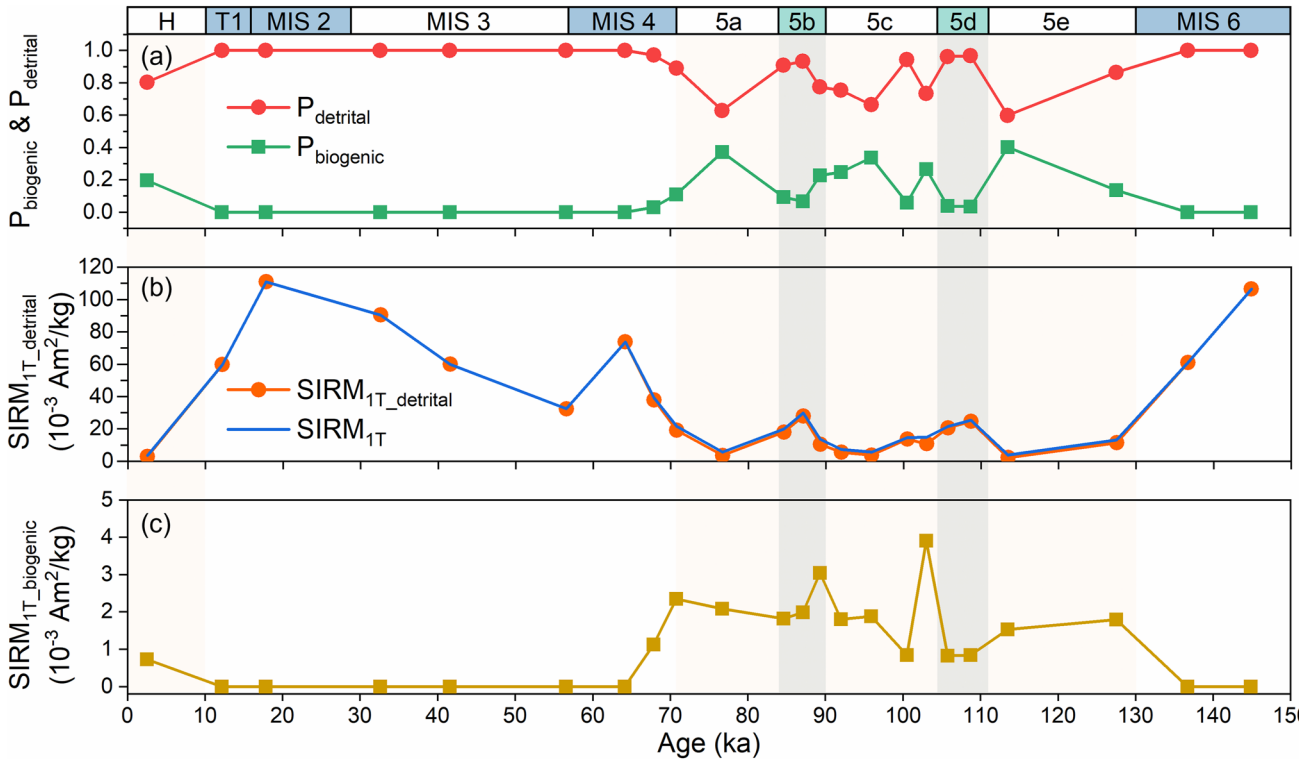

Figure 7. Temporal variations of biogenic (i.e., magnetofossils) and detrital magnetic minerals for the core MD11-3353 over the past 150 Kyr. (a) Relative content of biogenic ($P_{biogenic}$) and detrital ($P_{detrital}$) magnetic minerals. (b) $SIRM_{1T}$ and $SIRM_{1T}$ carried by detrital magnetic minerals ($SIRM_{1T\_detrital}$). (c) $SIRM_{1T}$ carried by biogenic magnetic minerals ($SIRM_{1T\_biogenic}$) (see text).

estimate the temporal variations of biogenic and detrital magnetic minerals across the core MD11-3353 on the basis of the following formula (Dunlop, 2002).

$$(M_{rs}/M_s)_{sample} = P_{biogenic}(M_{rs}/M_s)_{biogenic} + P_{detrital}(M_{rs}/M_s)_{detrital}$$

where $(M_{rs}/M_s)_{sample}$ represents the remanence ratio of one targeted sample, $P_{biogenic}$ is the percentage of biogenic magnetites (i.e., magnetofossils) in the sample, $P_{detrital}$ (i.e., $1 - P_{biogenic}$) is the percentage of detrital magnetic minerals in the sample, $(M_{rs}/M_s)_{biogenic}$ is the remanence ratio related to magnetofossils, and $(M_{rs}/M_s)_{detrital}$ is the remanence ratio related to detrital magnetic minerals. We gave an assumed value of 0.44 to $(M_{rs}/M_s)_{biogenic}$ on the basis of an experimental value for partially collapsed and weakly interacting magnetosome chains (Li et al., 2012). The $(M_{rs}/M_s)_{detrital}$ value (0.2157 ± 0.0023) was calculated as the average of the value from eight glacial samples (i.e., S2-1, S2-2, S3-1, S3-2, S3-3, S4-1, S6-1, and S6-2), dominated by detrital titanomagnetites with nearly identical M_{rs}/M_s values. By this means, we roughly obtained the relative content of biogenic ($P_{biogenic}$) and detrital ($P_{detrital}$) magnetic minerals (Table S2 in Supporting Information S1). The results show that the temporal variations of the relative content of magnetofossils are consistent with that of the magnetic parameters κ_{ARM}/κ, B_c, B_{cr}, M_{rs}/M_s, and δ_{FC}/δ_{ZFC} (Figure 7a). The $SIRM_{1T}$ resulting from the contribution of biogenic ($SIRM_{1T\_biogenic}$) and detrital ($SIRM_{1T\_detrital}$) magnetic minerals was then calculated by $P_{biogenic} \times SIRM_{1T}$ and $P_{detrital} \times SIRM_{1T}$ (Table S2 in Supporting Information S1). The $SIRM_{1T\_detrital}$ curve nearly overlaps the $SIRM_{1T}$ one (Figure 7b), while the $SIRM_{1T\_biogenic}$ curve shows a gradual increase from MIS 6 to MIS 5 and a gradual decrease from MIS 5 to early MIS 4. It appears to be higher during the transition between relatively warm substage MIS 5c and the cold substages MIS 5d/MIS 5b (Figure 7c). Consistently with rock magnetic measurements and electron microscopic observations, these calculations therefore confirm that the magnetic fraction in core MD11-3353 consists over the last 150 Kyr of a high input in detrital magnetic minerals during the glacial periods and of both a low input in detrital magnetic minerals and a local production of magnetofossils during the interglacial periods.

Correlation analyses show that κ is linearly correlated with the abundance of detrital magnetic minerals (Figure 8a), but it is not correlated with the abundance of magnetofossils (Figure 8b). Indeed, SIRM1T_biogenic

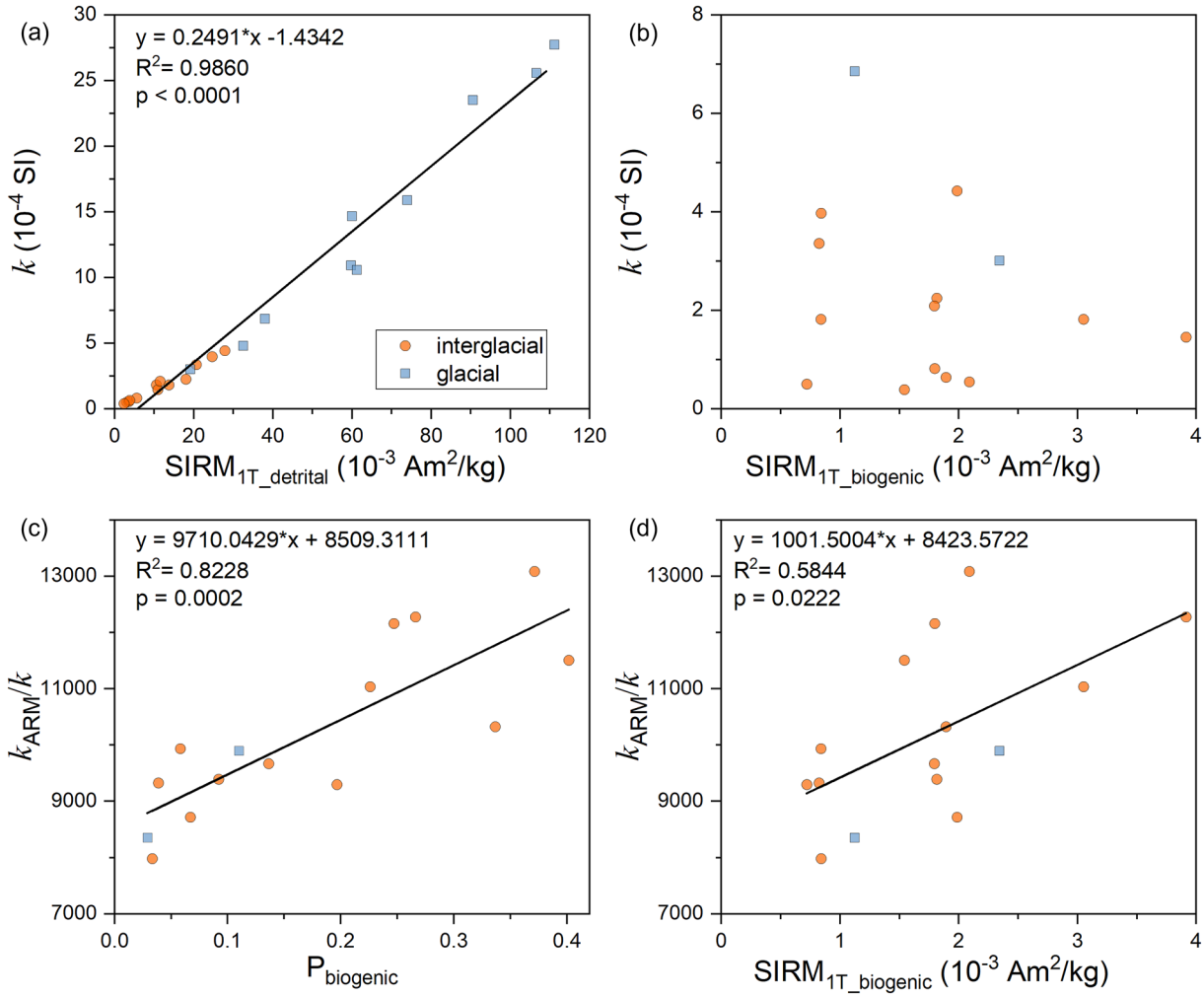

Figure 8. Correlation analyses between the magnetic parameters κ, κ_{ARM}/κ and the contents in biogenic (magnetofossils) and detrital magnetic minerals. (a) $SIRM_{1T\_detrital}$ versus κ. (b) $SIRM_{1T\_biogenic}$ versus κ. (c) $P_{biogenic}$ versus κ_{ARM}/κ. (d) $SIRM_{1T\_biogenic}$ versus κ_{ARM}/κ. In panel (a), the data of all the 23 selected samples were used, while in panels (b–d), the data of sediment samples from the interglacial periods (yellow solid circles) and the early MIS 4 (light blue solid squares) were used.

is much lower than SIRM1T_detrital indicating that the concentration variability of magnetic minerals in the sequence is mainly controlled by detrital input. The magnetic grain size parameter κ_{ARM}/κ is linearly correlated to the relative content of magnetofossils (Figure 8c). This confirms previous findings that the κ_{ARM}/κ could be used as reliable proxy for relative content of magnetofossils in marine sediments (Larrasoaña et al., 2012; S. Z. Liu et al., 2015; Yamazaki, 2012). Moreover, for core MD11-3353, we also observe that κ_{ARM}/κ is roughly linearly related to the abundance of magnetofossils (Figure 8d). This suggests that the magnetic parameters κ and κ_{ARM}/κ can be used as reliable proxies for recording the temporal variations of detrital magnetic minerals and magnetofossils, respectively, at least in core MD11-3353.

4.2. Magnetic Mineral Records in the Southern Indian Ocean

In order to get a large geographical view of the temporal evolution of the magnetic mineral composition in sediments from the Southern Indian Ocean, we compared our κ and κ_{ARM}/κ results to that of cores MD00-2375G and MR03K04-PC5. The concentration-dependent parameter κ shows similar temporal variations from one core to another with systematically higher values during the glacial periods than during the interglacial periods (Figures 9a–9c). This pattern is also similar to that of the South Atlantic, the Southwest Pacific, and dust records in Antarctic ice cores (Dezileau et al., 2000; Petit et al., 1990; Pugh et al., 2009; Schmieder et al., 2000), showing that the same pattern is prevailing on a large geographical scale in the SO. On the other hand, while κ_{ARM}/κ

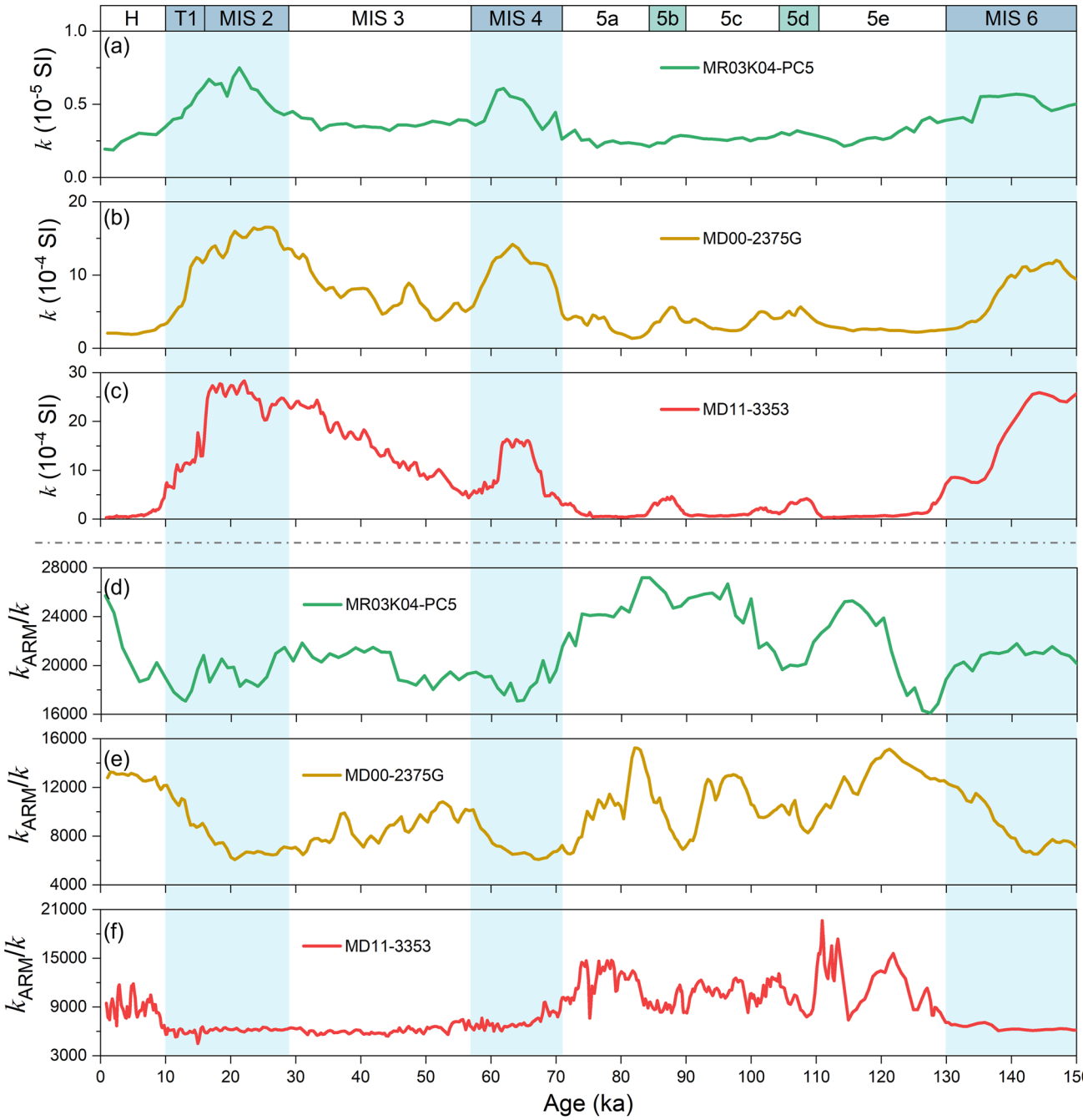

Figure 9. Comparison of temporal variations of magnetic parameters κ (a–c) and κ_{ARM}/κ (d–f) from core MR03K04-PC5 (a, d) (Yamazaki & Ikehara, 2012 and unpublished data), the MD00-2375G (b, e) (Mazaud et al., 2010), and core MD11-3353 (c, f) (this study) over the past 150 Kyr. Light blue shadings outline the glacial periods MIS 6, MIS 4, MIS 2, and T1.

systematically indicates coarser grains during the glacial periods with respect to interglacials, the short-term variations are not identical among the three cores (Figures 9d–9f). For instance, κ_{ARM}/κ is more or less anticorrelated to the κ records during both glacial and interglacial periods in both cores MD00-2375G and MR03K04-PC5, while κ_{ARM}/κ in core MD11-3353 is uniformly low during glacial periods and fluctuates around higher values during the interglacial periods. This suggests that the magnetic mineral assemblages could also be affected by local environments in the SO.

From a set of cores located east of the KP, Dezileau et al. (2000) showed that the detrital particles among which the magnetic ones are mainly of volcanogenic origin (i.e., from the Crozet and Kerguelen slopes), and their

lateral eastward transport is related to the ACC with an enhanced intensity during the glacial periods. This was confirmed by Mazaud et al. (2010) for core MD00-2375G, located north of the SAF and east of the KP, downstream with respect to the Kerguelen detrital source (Figure 1a). Core MR03K04-PC5 is slightly to the North and farther from the KP than core MD00-2375G. The decrease in the average sedimentation rate from the most proximal core MD11-3353 (∼7.5 cm/Kyr), to core MD00-2375G (∼4 cm/Kyr) to, finally, the most distal core MR03K04-PC5 (∼1.5 cm/Kyr) maybe also at the limit of the ACC influence confirms this unique detrital source and a progressive transport and deposition downstream. In this context, it is also reasonable to observe that the magnetic concentration (κ records, Figures 9a–9c) is getting smoother and lower from MD11-3353 to MD00-2375G and to core MR03K04-PC5.

In core MR03K04-PC5, Yamazaki and Ikehara (2012) observed abundant magnetofossils in the both glacial and interglacial periods, with systematically higher biogenic magnetite content during the glacial periods over the last 450 ka. The authors interpreted this as the result of iron fertilization, associated with an increased ocean productivity, in turn fueled by an increased eolian dust flux as this has been invoked for much older periods by Roberts et al. (2011). This core is located at 41°S, therefore north of the present SAF, with little amounts of detrital particles from the islands and more subjected to eolian dust fluxes. In core MD11-3353, we observe the opposite (i.e., more biogenic magnetite during interglacials) and it indicates that the mechanism proposed by Yamazaki and Ikehara (2012) cannot account for the variations in magnetofossils growth at the site of core MD11-3353. We suspect that the content and assemblage of magnetic minerals in this core have two different origins associated to two different climatic mechanisms that we shall discuss below.

4.3. The Climate-Driven Controlled Magnetic Records in the SIO

It has been suggested that a reliable proxy to identify eolian dust supply in marine sediment is the absolute concentration in hematite (Dinarès-Turell et al., 2003; Larrasoaña et al., 2012; Q. S. Liu et al., 2012; Roberts et al., 2011; Yamazaki & Ioka, 1997). Previous studies have suggested that the eolian dust input is far from sufficient to be a dominant source of terrigenous fluxes in the marine sediment cores of the SIO (Dezileau et al., 2000; Manoj et al., 2012; Mazaud et al., 2007, 2010). Although our results reveal that detrital titanomagnetites are dominant magnetic minerals in core MD11-3353 over the past 150 Kyr, small amounts of high-coercivity magnetic minerals such as hematite are also present. Their abundance (HIRM in Figure 2e) covaries with the other magnetic parameters such as κ, ARM, M_s, and $SIRM_{1T}$ (Figures 2a–2d) and also with the global temperature (Lisiecki & Raymo, 2005) and EDC dust flux (Lambert et al., 2008) (Figures 10a–10c). This suggests that, in core MD11-3353, hematite is part of the detrital magnetic assemblage which consistently record the temporal variations of the ACC and SHWW, that is, an enhancement of the ACC intensity and the SHWW stress during the glacial periods over the past 150 Kyr.

Biogenic magnetic minerals have been detected in core MD11-3353 during the interglacial periods. The κ_{ARM}/κ ratio among the magnetic parameters showing higher abundance of magnetofossils during the interglacial periods, matches well with the diatom-bound $\delta^{15}N$ records (Ai et al., 2020) and the Opal flux records (Thöle et al., 2019; Figures 10d–10f). We therefore interpret increased magnetofossil content as the result of the southward migration of the APF front during the interglacial periods (Ai et al., 2020; Civel-Mazens et al., 2021). Indeed, this promoted an increase of the SO upwelling strength that enhanced the transport of more organic matter, sulfate, and other nutrients. Nutrient availability and relatively warm environments promoted MTB blooms, which may have particularly stimulated proliferation of dissimilatory sulfate-reducing MTB (Li et al., 2022, 2021) that are well known to produce straight bullet-shaped magnetite magnetosomes (Li, Menguy, Roberts, et al., 2020; Pósfai et al., 2013). In contrast, due to the northward migration of the APF during the glacial periods, the SO upwelling position could have not impacted the KP region, which resulted in a local nutrient deficiency and limited MTB proliferation (Civel-Mazens et al., 2021; Thöle et al., 2019). Therefore, our results indicate that MTB blooming and subsequent magnetofossils preservation at the site of core MD11-3353 could be stimulated by organic matter related to the SO upwelling, rather than iron fertilization related to eolian dust fluxes. Consequently, we can conclude that magnetofossil record in core MD11-3353 reflects the temporal variations of the SO upwelling and the latitudinal migration of the APF over the past 150 Kyr.

5. Conclusions

The combination of rock magnetic measurements and electron microscopic observations on core MD11-3353 from the SIO reveals the climate-controlled variations of detrital and biogenic magnetic minerals over the

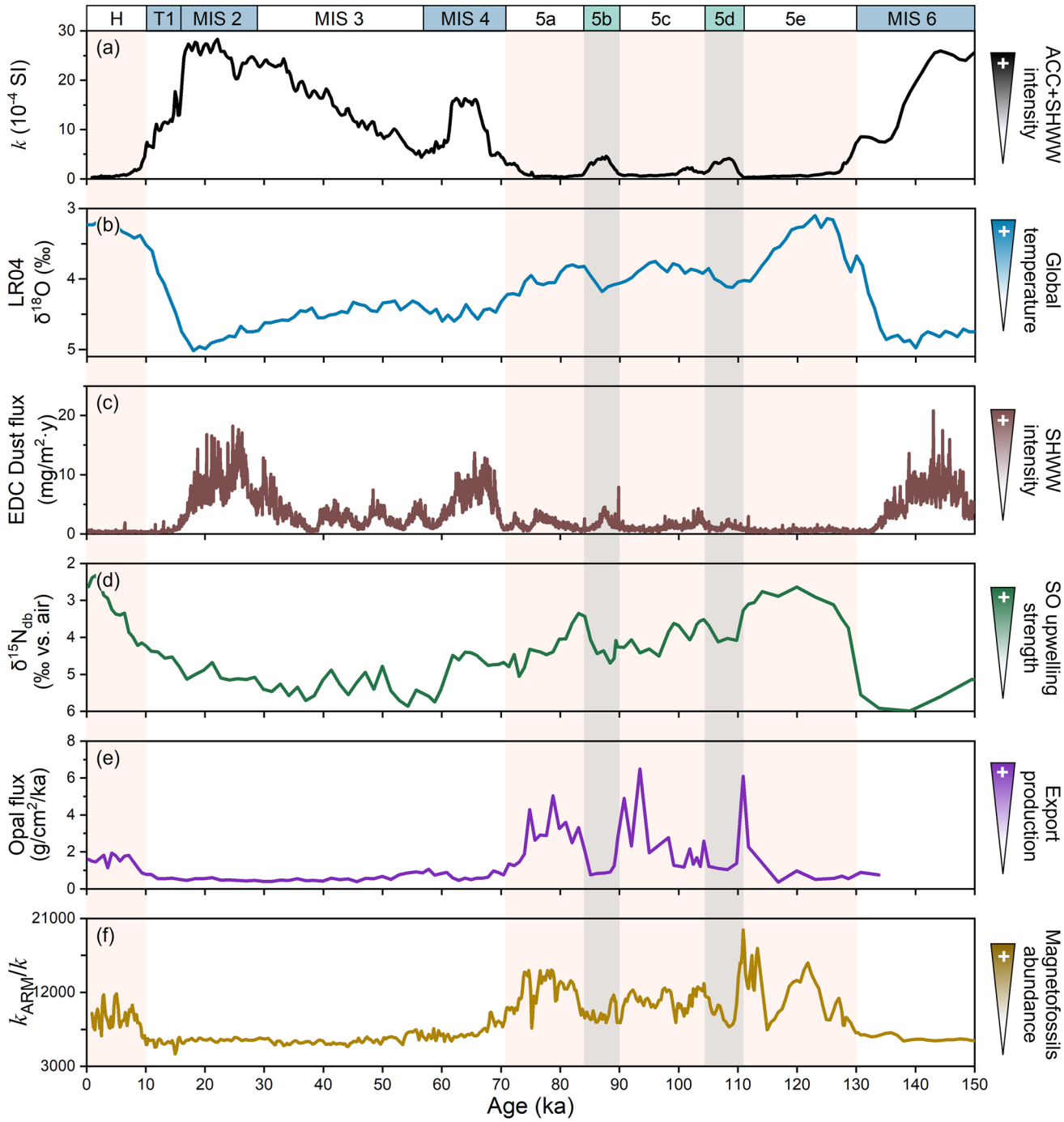

Figure 10. Temporal variations of global temperature, magnetic records, SO upwelling strength, export production from core MD11-3353 for the past 150 Kyr. (a) κ from core MD11-3353 (this study). (b) LR04 benthic δ^{18}O stack (Lisiecki & Raymo, 2005). (c) Dust flux of EPICA Dome C (EDC) ice core (Lambert et al., 2008). (d) Diatom-bound δ^{15}N records from core MD11-3353 (Ai et al., 2020). (e) Opal flux from core MD11-3353 (Thöle et al., 2019). (f) κ_{ARM}/κ from core MD11-3353 (this study). Light pink shadings outline the interglacial periods (i.e., MIS 5 and the Holocene), and gray shadings outline the cold substages MIS 5b and MIS 5d.

past 150 Kyr. During the glacial periods (MIS 6, MIS 4-2, and T1), the SHWW stress and the ACC intensity increases, the sea level drops, and both the current erosion and eolian dust could enhance inducing an increase in detrital input mainly made of inorganic titanomagnetites with minor contribution of hematite. In contrast, during the interglacial periods (MIS 5 and the Holocene) with reduced detrital input due to a reduced ACC intensity, the increased SO upwelling strength, resulting from the southward migration of the APF, delivered

organic matter and other nutrients to the region southwest of the KP, stimulating MTB blooming and subsequent magnetofossil preservation.

Our results therefore suggest that the detrital magnetic minerals in core MD11-3353 record the temporal variations of the ACC intensity and the SHWW stress over the last climatic cycle, while the occurrence magnetofossils testify to the latitudinal variations of the APF and the strength of the SO upwelling in the SIO during interglacials.

Data Availability Statement

All of the data used to build Figures 2 and 4 and Figures S32–S35 in Supporting Information S1 of this paper are available in Li (2023).

Acknowledgments
We are grateful to the MD crew, who was able to collect long cores in rough seas! We also thank the Paul-Emile Victor Institute for organizing the cruise and chartered the MD. We are grateful to T. Yamazaki for providing his numerical data including the unpublished κ_{ARM}/κ ones. Liao Chang and Fabio Florindo very kindly accepted to review the version of the manuscript already revised on the basis of two anonymous referees' comments. This is quite unusual, and we really thank them as well as the two first referees, for their help in improving this article. This study was supported financially in China by the National Natural Science Foundation of China (Grants 42225402, 41920104009, and 41890843), Innovation Group Project of Southern Marine Science and Engineering Guangdong Laboratory (Zhuhai) (No. 311022004), the Key Research Program of the Institute of Geology and Geophysics, CAS, Grant IGGCAS-202202, and in France by the Laboratoire des Sciences du Climat et de l'Environnement. We thank the SEM and TEM engineers at the IGG-CAS (Beijing): Mr. Lixin Gu and Mr. Tang Xu, for smooth running of instruments.

References

Ai, X. E., Studer, A. S., Sigman, D. M., Martinez-Garcia, A., Fripiat, F., Thole, L. M., et al. (2020). Southern Ocean upwelling, Earth's obliquity, and glacial-interglacial atmospheric CO_2 change. *Science*, *370*(6522), 1348–1352. https://doi.org/10.1126/science.abd2115

Anderson, R. F., Ali, S., Bradtmiller, L. I., Nielsen, S. H. H., Fleisher, M. Q., Anderson, B. E., & Burckle, L. H. (2009). Wind-driven upwelling in the Southern Ocean and the deglacial rise in atmospheric CO_2. *Science*, *323*(5920), 1443–1448. https://doi.org/10.1126/science.1167441

Bareille, G., Grousset, F. E., Labracherie, M., Labeyrie, L. D., & Petit, J. R. (1994). Origin of detrital fluxes in the southeast Indian Ocean during the last climatic cycles. *Paleoceanography*, *9*(6), 799–819. https://doi.org/10.1029/94pa01946

Berndt, T. A., Chang, L., & Pei, Z. W. (2020). Mind the gap: Towards a biogenic magnetite palaeoenvironmental proxy through an extensive finite-element micromagnetic simulation. *Earth and Planetary Science Letters*, *532*, 116010. https://doi.org/10.1016/j.epsl.2019.116010

Breton, T., Nauret, F., Pichat, S., Moine, B., Moreira, M., Rose-Koga, E. F., et al. (2013). Geochemical heterogeneities within the Crozet hotspot. *Earth and Planetary Science Letters*, *376*, 126–136. https://doi.org/10.1016/j.epsl.2013.06.020

Chang, L., Harrison, R. J., & Berndt, T. A. (2019). Micromagnetic simulation of magnetofossils with realistic size and shape distributions: Linking magnetic proxies with nanoscale observations and implications for magnetofossil identification. *Earth and Planetary Science Letters*, *527*, 115790. https://doi.org/10.1016/j.epsl.2019.115790

Chang, L., Harrison, R. J., Zeng, F., Berndt, T. A., Roberts, A. P., Heslop, D., & Zhao, X. (2018). Coupled microbial bloom and oxygenation decline recorded by magnetofossils during the Palaeocene–Eocene Thermal Maximum. *Nature Communications*, *9*(1), 4007. https://doi.org/10.1038/s41467-018-06472-y

Chang, L., Heslop, D., Roberts, A. P., Rey, D., & Mohamed, K. J. (2016). Discrimination of biogenic and detrital magnetite through a double Verwey transition temperature. *Journal of Geophysical Research: Solid Earth*, *121*(1), 3–14. https://doi.org/10.1002/2015JB012485

Chang, L., Hoogakker, B. A., Heslop, D., Zhao, X., Roberts, A. P., De Deckker, P., et al. (2023). Indian Ocean glacial deoxygenation and respired carbon accumulation during mid-late Quaternary ice ages. *Nature Communications*, *14*(1), 4841. https://doi.org/10.1038/s41467-023-40452-1

Chang, L., Roberts, A. P., Heslop, D., Hayashida, A., Li, J. H., Zhao, X., et al. (2016). Widespread occurrence of silicate-hosted magnetic mineral inclusions in marine sediments and their contribution to paleomagnetic recording. *Journal of Geophysical Research: Solid Earth*, *121*(12), 8415–8431. https://doi.org/10.1002/2016JB013109

Cisowski, S. (1981). Interacting vs. non-interacting single domain behavior in natural and synthetic samples. *Physics of the Earth and Planetary Interiors*, *26*(1–2), 56–62. https://doi.org/10.1016/0031-9201(81)90097-2

Civel-Mazens, M., Crosta, X., Cortese, G., Michel, E., Mazaud, A., Ther, O., et al. (2021). Antarctic Polar Front migrations in the Kerguelen Plateau region, Southern Ocean, over the past 360 kyrs. *Global and Planetary Change*, *202*, 103526. https://doi.org/10.1016/j.gloplacha.2021.103526

Day, R., Fuller, M., & Schmidt, V. A. (1977). Hysteresis properties of titanomagnetites: Grain-size and compositional dependence. *Physics of the Earth and Planetary Interiors*, *13*(4), 260–267. https://doi.org/10.1016/0031-9201(77)90108-x

Dezileau, L., Bareille, G., Reyss, J. L., & Lemoine, F. (2000). Evidence for strong sediment redistribution by bottom currents along the southeast Indian ridge. *Deep Sea Research Part I*, *47*(10), 1899–1936. https://doi.org/10.1016/s0967-0637(00)00008-x

Dinarès-Turell, J., Hoogakker, B. A. A., Roberts, A. P., Rohling, E. J., & Sagnotti, L. (2003). Quaternary climatic control of biogenic magnetite production and eolian dust input in cores from the Mediterranean Sea. *Palaeogeography, Palaeoclimatology, Palaeoecology*, *190*, 195–209. https://doi.org/10.1016/s0031-0182(02)00605-3

Dunlop, D. J. (2002). Theory and application of the Day plot (M_{rs}/M_s versus H_{cr}/H_c) 1. Theoretical curves and tests using titanomagnetite data. *Journal of Geophysical Research*, *107*(B3), 2056. https://doi.org/10.1029/2001JB000486

Egli, R. (2004). Characterization of individual rock magnetic components by analysis of remanence curves, 1. Unmixing natural sediments. *Studia Geophysica et Geodaetica*, *48*(2), 391–446. https://doi.org/10.1023/B:SGEG.0000020839.45304.6d

Egli, R. (2013). VARIFORC: An optimized protocol for calculating non-regular first-order reversal curve (FORC) diagrams. *Global and Planetary Change*, *110*, 302–320. https://doi.org/10.1016/j.gloplacha.2013.08.003

Egli, R., Chen, A. P., Winklhofer, M., Kodama, K. P., & Horng, C. S. (2010). Detection of noninteracting single domain particles using first-order reversal curve diagrams. *Geochemistry, Geophysics, Geosystems*, *11*(1), Q01Z11. https://doi.org/10.1029/2009GC002916

Graham, R. M., de Boer, A. M., Heywood, K. J., Chapman, M. R., & Stevens, D. P. (2012). Southern Ocean fronts: Controlled by wind or topography? *Journal of Geophysical Research: Oceans*, *117*(C8), C08018. https://doi.org/10.1029/2012jc007887

Harrison, R. J., & Feinberg, J. M. (2008). FORCinel: An improved algorithm for calculating first-order reversal curve distributions using locally weighted regression smoothing. *Geochemistry, Geophysics, Geosystems*, *9*(5), Q05016. https://doi.org/10.1029/2008GC001987

Heslop, D., Dekkers, M. J., Kruiver, P. P., & van Oorschot, I. H. M. (2002). Analysis of isothermal remanent magnetization acquisition curves using the expectation-maximization algorithm. *Geophysical Journal International*, *148*(1), 58–64. https://doi.org/10.1046/j.0956-540x.2001.01558.x

Homrighausen, S., Hoernle, K., Wartho, J. A., Hauff, F., & Werner, R. (2021). Do the 85°E Ridge and Conrad Rise form a hotspot track crossing the Indian Ocean? *Lithos*, *398–399*, 106234. https://doi.org/10.1016/j.lithos.2021.106234

Jiang, X. D., Zhao, X. Y., Zhao, X., Jiang, Z. X., Chou, Y. M., Zhang, T. W., et al. (2021). Quantifying contributions of magnetic inclusions within silicates to marine sediments: A dissolution approach to isolating volcanic signals for improved paleoenvironmental reconstruction. *Journal of Geophysical Research: Solid Earth*, *126*(10), e2021JB022680. https://doi.org/10.1029/2021JB022680

Jouzel, J., Masson-Delmotte, V., Cattani, O., Dreyfus, G., Falourd, S., Hoffmann, G., et al. (2007). Orbital and millennial Antarctic climate variability over the past 800,000 years. *Science*, *317*(5839), 793–796. https://doi.org/10.1126/science.1141038

King, J. W., & Channell, J. E. T. (1991). Sedimentary magnetism, environmental magnetism, and magnetostratigraphy. *Reviews of Geophysics*, *29*(S1), 358–370. https://doi.org/10.1002/rog.1991.29.s1.358

Kirschvink, J. L., & Chang, S. B. R. (1984). Ultrafine-grained magnetite in deep-sea sediments: Possible bacterial magnetofossils. *Geology*, *12*(9), 559–562. https://doi.org/10.1130/0091-7613(1984)12<559:UMIDSP>2.0.CO;2

Kohfeld, K. E., Graham, R. M., de Boer, A. M., Sime, L. C., Wolff, E. W., Le Quere, C., & Bopp, L. (2013). Southern Hemisphere westerly wind changes during the Last Glacial Maximum: Paleo-data synthesis. *Quaternary Science Reviews*, *68*, 76–95. https://doi.org/10.1016/j.quascirev.2013.01.017

Kohfeld, K. E., Le Quere, C., Harrison, S. P., & Anderson, R. F. (2005). Role of marine biology in glacial-interglacial CO_2 cycles. *Science*, *308*(5718), 74–78. https://doi.org/10.1126/science.1105375

Kopp, R. E., & Kirschvink, J. L. (2008). The identification and biogeochemical interpretation of fossil magnetotactic bacteria. *Earth-Science Reviews*, *86*(1–4), 42–61. https://doi.org/10.1016/j.earscirev.2007.08.001

Kruiver, P. P., Dekkers, M. J., & Heslop, D. (2001). Quantification of magnetic coercivity components by the analysis of acquisition curves of isothermal remanent magnetisation. *Earth and Planetary Science Letters*, *189*(3–4), 269–276. https://doi.org/10.1016/S0012-821X(01)00367-3

Lambert, F., Delmonte, B., Petit, J. R., Bigler, M., Kaufmann, P. R., Hutterli, M. A., et al. (2008). Dust-climate couplings over the past 800,000 years from the EPICA Dome C ice core. *Nature*, *452*(7187), 616–619. https://doi.org/10.1038/nature06763

Larrasoaña, J. C., Roberts, A. P., Chang, L., Schellenberg, S. A., Fitz Gerald, J. D., Norris, R. D., & Zachos, J. C. (2012). Magnetotactic bacterial response to Antarctic dust supply during the Palaeocene–Eocene thermal maximum. *Earth and Planetary Science Letters*, *333–334*, 122–133. https://doi.org/10.1016/j.epsl.2012.04.003

Li, J. H. (2023). Glacial-interglacial circulation and climatic changes in the South Indian Ocean (Kerguelen Plateau region) recorded by detrital and biogenic magnetic minerals [Dataset]. Figshare. https://doi.org/10.6084/m9.figshare.22189276.v6

Li, J. H., Benzerara, K., Bernard, S., & Beyssac, O. (2013). The link between biomineralization and fossilization of bacteria: Insights from field and experimental studies. *Chemical Geology*, *359*, 49–69. https://doi.org/10.1016/j.chemgeo.2013.09.013

Li, J. H., Liu, P. Y., Menguy, N., Benzerara, K., Bai, J. L., Zhao, X., et al. (2022). Identification of sulfate-reducing magnetotactic bacteria via a group-specific 16S rDNA primer and correlative fluorescence and electron microscopy: Strategy for culture-independent study. *Environmental Microbiology*, *24*(11), 5019–5038. https://doi.org/10.1111/1462-2920.16109

Li, J. H., Liu, P. Y., Tamaxia, A., Zhang, H., Liu, Y., Wang, J., et al. (2021). Diverse intracellular inclusion types within magnetotactic bacteria: Implications for biogeochemical cycling in aquatic environments. *Journal of Geophysical Research: Biogeosciences*, *126*(7), e2021JG006310. https://doi.org/10.1029/2021jg006310

Li, J. H., Liu, P. Y., Wang, J., Roberts, A. P., & Pan, Y. X. (2020). Magnetotaxis as an adaptation to enable bacterial shuttling of microbial sulfur and sulfur cycling across aquatic oxic-anoxic interfaces. *Journal of Geophysical Research: Biogeosciences*, *125*(12), e2020JG006012. https://doi.org/10.1029/2020jg006012

Li, J. H., Liu, Y., Liu, S. C., Roberts, A. P., Pan, H. M., Xiao, T., & Pan, Y. X. (2020). Classification of a complexly mixed magnetic mineral assemblage in Pacific Ocean surface sediment by electron microscopy and supervised magnetic unmixing. *Frontiers in Earth Science*, *8*, 609058. https://doi.org/10.3389/feart.2020.609058

Li, J. H., Menguy, N., Leroy, E., Roberts, A. P., Liu, P. Y., & Pan, Y. X. (2020). Biomineralization and magnetism of uncultured magnetotactic coccus strain THC-1 with non-chained magnetosomal magnetite nanoparticles. *Journal of Geophysical Research: Solid Earth*, *125*(12), e2020JB020853. https://doi.org/10.1029/2020jb020853

Li, J. H., Menguy, N., Roberts, A. P., Gu, L., Leroy, E., Bourgon, J., et al. (2020). Bullet-shaped magnetite biomineralization within a magnetotactic Deltaproteobacterium: Implications for magnetofossil identification. *Journal of Geophysical Research: Biogeosciences*, *125*(7), e2020JG005680. https://doi.org/10.1029/2020jg005680

Li, J. H., Wu, W. F., Liu, Q. S., & Pan, Y. X. (2012). Magnetic anisotropy, magnetostatic interactions and identification of magnetofossils. *Geochemistry, Geophysics, Geosystems*, *13*(12), 16. https://doi.org/10.1029/2012GC004384

Lisiecki, L. E., & Raymo, M. E. (2005). A Pliocene-Pleistocene stack of 57 globally distributed benthic $\delta^{18}O$ records. *Paleoceanography*, *20*(1), PA1003. https://doi.org/10.1029/2004PA001071

Liu, P. Y., Yue, Z., Rong, Z. R., Bai, J. L., Zhu, K. L., Benzerara, K., et al. (2022). Key gene networks that control magnetosome biomineralization in magnetotactic bacteria. *National Science Review*, *10*(1), nwac238. https://doi.org/10.1093/nsr/nwac238/6779695

Liu, Q. S., Roberts, A. P., Larrasoaña, J. C., Banerjee, S. K., Guyodo, Y., Tauxe, L., & Oldfield, F. (2012). Environmental magnetism: Principles and applications. *Reviews of Geophysics*, *50*(4), RG4002. https://doi.org/10.1029/2012RG000393

Liu, S. Z., Deng, C. L., Xiao, J. L., Li, J. H., Paterson, G. A., Chang, L., et al. (2015). Insolation driven biomagnetic response to the Holocene Warm Period in semi-arid East Asia. *Scientific Reports*, *5*(1), 8001. https://doi.org/10.1038/srep08001

Manoj, M. C., Thamban, M., Basavaiah, N., & Mohan, R. (2012). Evidence for climatic and oceanographic controls on terrigenous sediment supply to the Indian Ocean sector of the Southern Ocean over the past 63,000 years. *Geo-Marine Letters*, *32*(3), 251–265. https://doi.org/10.1007/s00367-011-0267-6

Marshall, J., & Speer, K. (2012). Closure of the meridional overturning circulation through Southern Ocean upwelling. *Nature Geoscience*, *5*(3), 171–180. https://doi.org/10.1038/ngeo1391

Mazaud, A., Kissel, C., Laj, C., Sicre, M. A., Michel, E., & Turon, J. L. (2007). Variations of the ACC-CDW during MIS3 traced by magnetic grain deposition in midlatitude South Indian Ocean cores: Connections with the northern hemisphere and with central Antarctica. *Geochemistry, Geophysics, Geosystems*, *8*(5), Q05012. https://doi.org/10.1029/2006gc001532

Mazaud, A., & Michel, E. (2011). *MD185 INDIEN SUD-1 cruise report*. RV Marion Dufresne.

Mazaud, A., Michel, E., Dewilde, F., & Turon, J. L. (2010). Variations of the Antarctic Circumpolar Current intensity during the past 500 ka. *Geochemistry, Geophysics, Geosystems*, *11*(8), Q08007. https://doi.org/10.1029/2010gc003033

McCave, I. N., Crowhurst, S. J., Kuhn, G., Hillenbrand, C. D., & Meredith, M. P. (2014). Minimal change in Antarctic Circumpolar Current flow speed between the last glacial and Holocene. *Nature Geoscience*, *7*(2), 113–116. https://doi.org/10.1038/ngeo2037

Moskowitz, B. M., Frankel, R. B., & Bazylinski, D. A. (1993). Rock magnetic criteria for the detection of biogenic magnetite. *Earth and Planetary Science Letters*, *120*(3–4), 283–300. https://doi.org/10.1016/0012-821X(93)90245-5

Munday, D. R., Johnson, H. L., & Marshall, D. P. (2013). Eddy saturation of equilibrated circumpolar currents. *Journal of Physical Oceanography*, *43*(3), 507–532. https://doi.org/10.1175/jpo-d-12-095.1

Muxworthy, A. R., & McClelland, E. (2000). Review of the low-temperature magnetic properties of magnetite from a rock magnetic perspective. *Geophysical Journal International*, *140*(1), 101–114. https://doi.org/10.1046/j.1365-246x.2000.00999.x

Muxworthy, A. R., & Williams, W. (2009). Critical superparamagnetic/single-domain grain sizes in interacting magnetite particles: Implications for magnetosome crystals. *Journal of The Royal Society Interface*, *6*(41), 1207–1212. https://doi.org/10.1098/rsif.2008.0462

Paillard, D., Labeyrie, L., & Yiou, P. (1996). Macintosh Program performs time-series analysis. *Eos, Transactions American Geophysical Union*, *77*(39), 379. https://doi.org/10.1029/96EO00259

Palter, J. B., Marinov, I., Sarmiento, J. L., & Gruber, N. (2013). *Large-scale, persistent nutrient fronts of the world ocean: Impacts on biogeochemistry*. Springer Berlin Heidelberg.

Pan, Y. X., Petersen, N., Davila, A. F., Zhang, L. M., Winklhofer, M., Liu, Q. S., et al. (2005). The detection of bacterial magnetite in recent sediments of Lake Chiemsee (Southern Germany). *Earth and Planetary Science Letters*, *232*(1–2), 109–123. https://doi.org/10.1016/j.epsl.2005.01.006

Park, Y. H., Park, T., Kim, T. W., Lee, S. H., Hong, C. S., Lee, J. H., et al. (2019). Observations of the Antarctic Circumpolar Current over the Udintsev Fracture Zone, the narrowest choke point in the Southern Ocean. *Journal of Geophysical Research: Oceans*, *124*(7), 4511–4528. https://doi.org/10.1029/2019jc015024

Peters, C., & Dekkers, M. J. (2003). Selected room temperature magnetic parameters as a function of mineralogy, concentration and grain size. *Physics and Chemistry of the Earth, Parts A/B/C*, *28*(16), 659–667. https://doi.org/10.1016/S1474-7065(03)00120-7

Petit, J. R., Mounier, L., Jouzel, J., Korotkevich, Y. S., Kotlyakov, V. I., & Lorius, C. (1990). Palaeoclimatological and chronological implications of the Vostok core dust record. *Nature*, *343*(6253), 56–58. https://doi.org/10.1038/343056a0

Pike, C. R., Roberts, A. P., & Verosub, K. L. (1999). Characterizing interactions in fine magnetic particle systems using first order reversal curves. *Journal of Applied Physics*, *85*(9), 6660–6667. https://doi.org/10.1063/1.370176

Pósfai, M., Lefevre, C. T., Trubitsyn, D., Bazylinski, D. A., & Frankel, R. B. (2013). Phylogenetic significance of composition and crystal morphology of magnetosome minerals. *Frontiers in Microbiology*, *4*, 344. https://doi.org/10.3389/fmicb.2013.00344

Pugh, R. S., McCave, I. N., Hillenbrand, C. D., & Kuhn, G. (2009). Circum-Antarctic age modelling of Quaternary marine cores under the Antarctic Circumpolar Current: Ice-core dust–magnetic correlation. *Earth and Planetary Science Letters*, *284*(1–2), 113–123. https://doi.org/10.1016/j.epsl.2009.04.016

Ragueneau, O., Treguer, P., Leynaert, A., Anderson, R. F., Brzezinski, M. A., DeMaster, D. J., et al. (2000). A review of the Si cycle in the modem ocean: Recent progress and missing gaps in the application of biogenic opal as a paleoproductivity proxy. *Global and Planetary Change*, *26*(4), 317–365. https://doi.org/10.1016/s0921-8181(00)00052-7

Rintoul, S. R., & Naveira Garabato, A. C. (2013). Dynamics of the Southern Ocean circulation. In *Ocean circulation and climate—A 21st century perspective* (pp. 471–492).

Roberts, A. P. (2015). Magnetic mineral diagenesis. *Earth-Science Reviews*, *151*, 1–47. https://doi.org/10.1016/j.earscirev.2015.09.010

Roberts, A. P., Almeida, T. P., Church, N. S., Harrison, R. J., Heslop, D., Li, Y. L., et al. (2017). Resolving the origin of pseudo-single domain magnetic behavior. *Journal of Geophysical Research: Solid Earth*, *122*(12), 9534–9558. https://doi.org/10.1002/2017JB014860

Roberts, A. P., Chang, L., Heslop, D., Florindo, F., & Larrasoaña, J. C. (2012). Searching for single domain magnetite in the "pseudo-single-domain" sedimentary haystack: Implications of biogenic magnetite preservation for sediment magnetism and relative paleointensity determinations. *Journal of Geophysical Research*, *117*(B8), B08104. https://doi.org/10.1029/2012JB009412

Roberts, A. P., Florindo, F., Villa, G., Chang, L., Jovane, L., Bohaty, S. M., et al. (2011). Magnetotactic bacterial abundance in pelagic marine environments is limited by organic carbon flux and availability of dissolved iron. *Earth and Planetary Science Letters*, *310*(3–4), 441–452. https://doi.org/10.1016/j.epsl.2011.08.011

Roberts, A. P., Pike, C. R., & Verosub, K. L. (2000). First-order reversal curve diagrams: A new tool for characterizing the magnetic properties of natural samples. *Journal of Geophysical Research*, *105*(B12), 28461–428475. https://doi.org/10.1029/2000JB900326

Robertson, D. J., & France, D. E. (1994). Discrimination of remanence-carrying minerals in mixtures, using isothermal remanent magnetisation acquisition curves. *Physics of the Earth and Planetary Interiors*, *82*(3–4), 223–234. https://doi.org/10.1016/0031-9201(94)90074-4

Rojas, M., Moreno, P., Kageyama, M., Crucifix, M., Hewitt, C., Abe-Ouchi, A., et al. (2009). The Southern Westerlies during the last glacial maximum in PMIP2 simulations. *Climate Dynamics*, *32*(4), 525–548. https://doi.org/10.1007/s00382-008-0421-7

Saenko, O. A., Fyfe, J. C., & England, M. H. (2005). On the response of the oceanic wind-driven circulation to atmospheric CO_2 increase. *Climate Dynamics*, *25*(4), 415–426. https://doi.org/10.1007/s00382-005-0032-5

Schmieder, F., von Dobeneck, T., & Bleil, U. (2000). The Mid-Pleistocene climate transition as documented in the deep South Atlantic Ocean: Initiation, interim state and terminal event. *Earth and Planetary Science Letters*, *179*(3), 539–549. https://doi.org/10.1016/S0012-821X(00)00143-6

Sigman, D. M., & Boyle, E. A. (2000). Glacial/interglacial variations in atmospheric carbon dioxide. *Nature*, *407*(6806), 859–869. https://doi.org/10.1038/35038000

Studer, A. S., Sigman, D. M., Martínez-García, A., Thöle, L. M., Michel, E., Jaccard, S. L., et al. (2018). Increased nutrient supply to the Southern Ocean during the Holocene and its implications for the pre-industrial atmospheric CO_2 rise. *Nature Geoscience*, *11*(10), 756–760. https://doi.org/10.1038/s41561-018-0191-8

Thöle, L. M., Amsler, H. E., Moretti, S., Auderset, A., Gilgannon, J., Lippold, J., et al. (2019). Glacial-interglacial dust and export production records from the Southern Indian Ocean. *Earth and Planetary Science Letters*, *525*, 115716. https://doi.org/10.1016/j.epsl.2019.115716

Toggweiler, J. R., Russell, J. L., & Carson, S. R. (2006). Midlatitude westerlies, atmospheric CO_2, and climate change during the ice ages. *Paleoceanography*, *21*(2), PA2005. https://doi.org/10.1029/2005pa001154

Toyos, M. H., Lamy, F., Lange, C. B., Lembke-Jene, L., Saavedra-Pellitero, M., Esper, O., & Arz, H. W. (2020). Antarctic Circumpolar Current dynamics at the Pacific entrance to the Drake Passage over the past 1.3 million years. *Paleoceanography and Paleoclimatology*, *35*(7), e2019PA003773. https://doi.org/10.1029/2019pa003773

Weeks, R., Laj, C., Endignoux, L., Fuller, M., Roberts, A., Manganne, R., et al. (1993). Improvements in long-core measurement techniques: Applications in palaeomagnetism and palaeoceanography. *Geophysical Journal International*, *114*(3), 651–662. https://doi.org/10.1111/j.1365-246X.1993.tb06994.x

Whitechurch, H., Montigny, R., Sevigny, J. H., Storey, M., & Salters, V. J. M. (1992). K-Ar and $^{40}Ar/^{39}Ar$ ages of Central Kerguelen Plateau basalts. *Proceedings of the Ocean Drilling Program, Scientific Result*, *120*, 71–77.

Wu, S. Z., Lembke-Jene, L., Lamy, F., Arz, H. W., Nowaczyk, N., Xiao, W. S., et al. (2021). Orbital- and millennial-scale Antarctic Circumpolar Current variability in Drake Passage over the past 140,000 years. *Nature Communications*, *12*(1), 3948. https://doi.org/10.1038/s41467-021-24264-9

Yamazaki, T. (2008). Magnetostatic interactions in deep-sea sediments inferred from first-order reversal curve diagrams: Implications for relative paleointensity normalization. *Geochemistry, Geophysics, Geosystems*, *9*(2), Q02005. https://doi.org/10.1029/2007gc001797

Yamazaki, T. (2012). Paleoposition of the Intertropical Convergence Zone in the eastern Pacific inferred from glacial-interglacial changes in terrigenous and biogenic magnetic mineral fractions. *Geology*, *40*(2), 151–154. https://doi.org/10.1130/g32646.1

Yamazaki, T., Fu, W., Shimono, T., & Usui, Y. (2020). Unmixing biogenic and terrigenous magnetic mineral components in red clay of the Pacific Ocean using principal component analyses of first-order reversal curve diagrams and paleoenvironmental implications. *Earth Planets and Space*, *72*(1), 120. https://doi.org/10.1186/s40623-020-01248-5

Yamazaki, T., & Ikehara, M. (2012). Origin of magnetic mineral concentration variation in the Southern Ocean. *Paleoceanography*, *27*(2), PA2206. https://doi.org/10.1029/2011pa002271

Yamazaki, T., & Ioka, N. (1997). Cautionary note on magnetic grain-size estimation using the ratio of ARM to magnetic susceptibility. *Geophysical Research Letters*, *24*(7), 751–754. https://doi.org/10.1029/97GL00602

Yamazaki, T., & Kawahata, H. (1998). Organic carbon flux controls the morphology of magnetofossils in marine sediments. *Geology*, *26*(12), 1064–1066. https://doi.org/10.1130/0091-7613(1998)026<1064:OCFCTM>2.3.CO;2